AO-A217 731

MICROWAVE LABORATORY REPORT NO. 89-P-5

GaAs TRAVELING-WAVE OPTICAL MODULATORS USING MODULATED COPLANAR ELECTRODES WITH PERIODIC CROSS-TIE OVERLAYS

TECHNICAL REPORT

DTIC
COPY,
INSPECTED
I'

HAI-YOUNG LEE AND TATSUO ITOH

DECEMBER 1989

DTIC
ELECTE
S JAN 2 3 1990
E D

'on For
C°A&I
''B
'''ed
''ntion

THE UNIVERSITY OF TEXAS AT AUSTIN

DEPARTMENT OF ELECTRICAL ENGINEERING

AUSTIN, TEXAS 78712

By
Distr'...t'on/
Availability Codes
Dist   Avail and/or
        Special

A-1

REPORT DOCUMENTATION PAGE

1a. REPORT SECURITY CLASSIFICATION	1b. RESTRICTIVE MARKINGS
Unclassified	

2a. SECURITY CLASSIFICATION AUTHORITY	3. DISTRIBUTION / AVAILABILITY OF REPORT
2b. DECLASSIFICATION / DOWNGRADING SCHEDULE	Approved for public release; distribution unlimited.

4. PERFORMING ORGANIZATION REPORT NUMBER(S)	5. MONITORING ORGANIZATION REPORT NUMBER(S)
Microwave Laboratory Report No. 89-P-5	ARO 25045.32-EL

6a. NAME OF PERFORMING ORGANIZATION	6b. OFFICE SYMBOL (If applicable)	7a. NAME OF MONITORING ORGANIZATION
The University of Texas		U. S. Army Research Office

6c. ADDRESS (City, State, and ZIP Code)	7b. ADDRESS (City, State, and ZIP Code)
Dept. of Electrical & Computer Engineering Austin, TX 78712	P. O. Box 12211 Research Triangle Park, NC 27709-2211

8a. NAME OF FUNDING / SPONSORING ORGANIZATION	8b. OFFICE SYMBOL (If applicable)	9. PROCUREMENT INSTRUMENT IDENTIFICATION NUMBER
U. S. Army Research Office		DAAL03-88-K-0005

8c. ADDRESS (City, State, and ZIP Code)	10. SOURCE OF FUNDING NUMBERS			
	PROGRAM ELEMENT NO.	PROJECT NO.	TASK NO.	WORK UNIT ACCESSION NO
P. O. Box 12211 Research Triangle Park, NC 27709-2211				

11. TITLE (Include Security Classification)

GaAs Traveling-Wave Optical Modulators Using Modulated Coplanar Electrodes with Periodic Cross-Tie Overlays

12. PERSONAL AUTHOR(S)
Hai-Young Lee and Tatsuo Itoh

13a. TYPE OF REPORT	13b. TIME COVERED		14. DATE OF REPORT (Year, Month, Day)	15. PAGE COUNT
Technical	FROM	TO	Dec. 1989	

16. SUPPLEMENTARY NOTATION
The view, opinions and/or findings contained in this report are those of the author(s) and should not be construed as an official Department of the Army position, policy, or decision, unless so designated by other documentation.

17	COSATI CODES		18. SUBJECT TERMS (Continue on reverse if necessary and identify by block number)
FIELD	GROUP	SUB-GROUP	Traveling-Wave, Optical Modulator, Modulated Coplanar, Slow-Wave, Cross-Tie, Coplanar Strip Feeding

19 ABSTRACT (Continue on reverse if necessary and identify by block number)

This technical report describes traveling-wave optical modulators using cross-tie slow-wave electrodes on GaAs substrates as well as wideband feeding of a coplanar strip electrode. Phase velocity matching between modulation and optical waves is satisfied over a very wide bandwidth using the slow-wave electrodes. A new monolithic feeding method for the coplanar strip electrode has been developed by inserting an intermediate microstrip line between the coplanar strip and a feeding coaxial line.

20 DISTRIBUTION / AVAILABILITY OF ABSTRACT	21. ABSTRACT SECURITY CLASSIFICATION
☐ UNCLASSIFIED/UNLIMITED ☐ SAME AS RPT. ☐ DTIC USERS	Unclassified

22a NAME OF RESPONSIBLE INDIVIDUAL	22b. TELEPHONE (Include Area Code)	22c. OFFICE SYMBOL

DD FORM 1473, 84 MAR   83 APR edition may be used until exhausted.   SECURITY CLASSIFICATION OF THIS PAGE
All other editions are obsolete.

UNCLASSIFIED

GaAs TRAVELING-WAVE OPTICAL MODULATORS USING MODULATED COPLANAR ELECTRODES WITH PERIODIC CROSS-TIE OVERLAYS

This technical report describes traveling-wave optical modulators using cross-tie slow-wave electrodes on GaAs substrates as well as wideband feeding of a coplanar strip electrode. Periodic cross-tie conductors are overlaid on a modulated coplanar strip and a modulated coplanar waveguide electrode to make slow-wave electrodes.

In these structures, phase velocity matching between modulation and optical waves is satisfied over a very wide bandwidth by reducing the phase velocity of the modulation wave using the slow-wave electrodes. Therefore, the modulation bandwidths are greatly increased while the dominant conductor losses are relatively high and limit the bandwidths. The coplanar strip slow-wave structure has been build on a semi-insulating GaAs substrate and measured using a microwave network analyzer. The measured phase velocity is much lower than those of conventional coplanar electrodes and agrees very well with the calculated one.

In order to maintain the wide bandwidth in practical usage, a new feeding method for the coplanar strip electrode has been developed by inserting an intermediate microstrip line between the coplanar strip and a feeding coaxial line. The intermediate microstrip line greatly reduces reflections from the transitions and increases the feeding bandwidth. This feeding structure can be integrated monolithically with the optical modulators on a GaAs substrate.

TABLE OF CONTENTS

Chapter 1

Introduction

Very high-speed light modulations up to millimeter wave frequencies are required for high-bit rate optical communication and high-speed optical signal processing. Direct modulation of semiconductor lasers, however, is not effective in the high frequency regime due to spectral-line broadening of the laser diodes, and needs a short cavity to maintain a single longitudinal mode[1],[2]. On the other hand, external modulation of the laser diode using an optical modulator outside the cavity can be used effectively at such high frequencies while maintaining the single cavity mode and high purity spectral characteristics by isolating the laser cavity from the disturbance of the high-speed modulation.

Optical modulators using traveling-wave electrodes are especially useful for the high-speed external modulation. This is because the traveling-wave electrodes have inherently very wide bandwidth while the speed of lumped electrodes is limited by the charging time of the capacitance between the electrodes. The traveling-wave electrodes have high modulation depth as well, which increases with the active length of the device in the case of perfect velocity-matching between modulation wave and light wave. In the optimum design of a traveling-wave electro-optic modulator, the phase velocity matching between modulation and light waves is an essential task because the upper frequency limit is limited by the inverse of transit time difference between the two

1

waves[3]. Therefore, if the velocities of both the optical and modulation waves are equal to each other, the traveling-wave modulator would offer the potential of very wide modulation bandwidth and high modulation depth.

Conventional coplanar traveling-wave electrodes on typical electro-optic substrates, such as GaAs and LiNbO$_3$, cannot be designed for the velocity match[4]. In bulk LiNbO$_3$ crystal, phase velocity of the modulation wave is much slower than that of the light wave since the dielectric constant is much higher in microwave frequency region than in lightwave frequency region. Therefore, the phase velocity of the modulation wave must be increased using a fast-wave electrode which is not realizable currently over wide frequency range. On the other hand, although the dielectric constant of GaAs is almost the same in microwave and lightwave frequency regions, conventional coplanar electrodes on GaAs cannot be designed to achieve this phase velocity matching because the phase velocity of the modulation wave is higher than that of the light wave in any geometrical dimension due to the field traveling in the air side of the coplanar electrodes. Microstrip-type electrodes, which have a thin GaAs substrate between the two electrodes, satisfy the phase velocity matching since most of the modulation field is confined in the GaAs region. Unfortunately, the microstrip-type structures cannot be fabricated using current technologies since the very thin GaAs region cannot be grown on the electrode surface. A p-i-n structure[5] using a highly-doped region on a GaAs substrate for an electrode is limited by high losses of the modulation and optical waves. Deposition of a thick dielectric layer on the coplanar electrodes reduces not only the phase velocity of the modulation wave but also the characteristic impedance. Therefore, the thick dielectric layer results in wider electrode gap to maintain a given characteristic impedance such as 50 ohms of the outside

circuitry and then, the wider electrode gap requires higher modulation voltage. It is also difficult to build the thick dielectric layer of high quality.

Recently, a two-layer structure consisted of a thin $LiNbO_3$ layer on a thick dielectric substrate having a low dielectric constant has been proposed to satisfy the velocity matching condition[6]. Since the modulation wave in $LiNbO_3$ crystal is much slower than the light wave , the velocity of the modulation wave was increased using a thick substrate layer which has a low dielectric constant and supports the thin $LiNbO_3$ layer. However, such a two-layer structure is intrinsically dispersive because the modulation fields gradually concentrate into the upper $LiNbO_3$ layer of high dielectric constant with increasing frequency. In addition, the two-layer structure is not practical because the thin layer of single crystal $LiNbO_3$ cannot be grown on the dielectric substrate.

Aperiodic switched-electrode patterns have recently been used to compensate for the phase velocity mismatch in $LiNbO_3$ by aperiodically reversing the phase of the modulation wave[7]. Although the phase reversal method improves the bandwidth and the figure-of-merit of Mach-Zehnder traveling-wave optical modulators, it has intrinsically nonlinear phase response to the modulation frequency and high ripple in the modulation passband. Therefore, the phase reversal method is suitable only for frequency-domain applications that tolerate the phase nonlinearity and the high ripple, where the phase information and the ripple can be calibrated out.

Until several years ago, $LiNbO_3$ modulators have been exclusively developed and commercially used for wideband light modulation. For last several years, the $LiNbO_3$ modulators have been rapidly progressed to Mach-Zehnder interferometers and

directional couplers with bandwidths in excess of 40 GHz. In that period, a big obstacle of successful development of GaAs modulators was the poor quality of GaAs material resulting in high optical losses. Now, with many recent improvements and developments in III-V technologies such as Molecular Beam Epitaxy (MBE), the high optical losses and many fabrication difficulties have been greatly reduced. The GaAs traveling-wave modulator has very good potential of high-speed modulation for next-generation light communication while electro-optic coefficient of GaAs is relatively small compared to LiNbO3. The low dielectric constant as well as the relatively small velocity mismatch of GaAs material are very attractive because they allow the narrow electrode gap to reduce the modulation voltage at a given characteristic impedance and make the phase velocity matching possible. Furthermore, waveguide modulators on III-V substrate offer obvious potential of monolithic integration with signal sources and electrical driver circuitry. Therefore, optical modulators based on III-V substrate are expected to take a superior position on high-speed and highly integrated opto-electronic circuits.

There are several GaAs traveling-wave optical modulators[5],[8],[9] published but none of them are made to satisfy the essential phase velocity matching. Therefore, they are eventually limited by walk-off between the modulation and light waves. The highest bandwidth(20 GHz) has been obtained using a coplanar strip electrode on GaAs ridge optical waveguide and the walk-off was still the eventual limit of the bandwidth[9]. Consequently, the walk-off problem must be solved also for the GaAs traveling-wave modulators in order to achieve the highest bandwidth and use the above-mentioned advantages effectively.

This technical report describes GaAs traveling-wave optical modulators using coplanar slow-wave electrodes as well as the wideband feeding of a coplanar strip electrode. A periodic array of metal conductors is overlaid on a modulated coplanar strip electrode and a modulated coplanar waveguide electrode to make the slow-wave electrodes. In these structures, the phase velocity matching has been satisfied over a very wide bandwidth by reducing the phase velocity of the modulation wave using the slow-wave electrode. Therefore, the modulation bandwidths are greatly increased while the dominant conductor losses are relatively high and limit the bandwidths. The high conductor losses are reduced by periodically modulating the electrode geometries. The figures-of-merit, the bandwidth divided by the modulation voltage, are much higher than those of conventional structures because of the successful matching of the phase velocity. For the experimental conformation, a coplanar strip slow-wave electrode has been build on a GaAs substrate. The phase velocity measured using microwave network analyzer is very slower than those of conventional coplanar electrodes and agrees very well with the calculated one.

Wideband feedings of the traveling-wave modulators are required to maintain the modulator bandwidths in practical usage. The wideband feeding of the coplanar waveguide electrode can be done easily by directly connecting a coaxial line to the electrode since both coplanar waveguide and coaxial line are unbalanced lines. On the other hand, the coplanar strip is a balanced line which cannot be directly fed by the coaxial line because of unbalancing effect. Therefore, a new feeding method for coplanar strip electrode has been developed by inserting an intermediate microstrip line

between the coplanar strip and the coaxial line. The intermediate microstrip line greatly reduced the unbalancing effect and the reflections at the feeding transitions.

Chapter 2

Concept and Analysis of the Periodic Slow-wave Structure

2.1 Introduction

Coplanar traveling-wave electrodes on a GaAs substrate have the modulation wave faster than the light wave in GaAs waveguide due to the field in the air side of the electrode. Therefore, the modulation wave must be slowed down to match the phase velocity to that of the light wave since the light wave in the GaAs waveguide has the phase velocity approximately given by the refractive index of the GaAs waveguide.

There are several schemes to make a slow-wave transmission structure in which electromagnetic waves travel in a phase velocity slower than the bulk phase velocity. Physical principle of the slow-wave structures is based on a separation of electric and magnetic energies. If the electric and magnetic energies are separated in a certain way, we can change the distributed line inductance (L) and capacitance (C) individually. Therefore, the phase velocity, which is inversely proportional to $\sqrt{LC}$, can be reduced by increasing the line inductance and capacitance. This however, is not the case of normal-line structures since both electric and magnetic energies exist simultaneously in the same region and coupled to each other. Therefore, we cannot increase both electric and magnetic energies simultaneously by simply changing the geometries of normal-line structures. For instance, a coaxial line filled with a given dielectric material has an almost constant phase velocity. That is because the distributed inductance and

7

capacitance have inverse relations to the cross-sectional geometry and then, the LC product is constant.

In microwave monolithic integrated circuits (MMIC), two typical slow-wave structures have been introduced to reduce guided wavelength as well as the circuit size for the high density of integration. Metal-Insulator-Semiconductor (MIS) slow-wave structure[10],[11] consists of metal strip lines on a doped semiconductor substrate spaced by a thin insulating layer. The separation of electric and magnetic energies is accomplished in the cross-sectional direction. The electric field concentrates mostly in the insulator region since the doped semiconductor does not allow the electric field lines pass through. The magnetic field passes through the semiconductor and most of the magnetic energy is stored in wide semiconductor region. Schottky contact slow-wave structure[12] uses a depletion region formed underneath metal strip lines on a semiconductor substrate. Electric field is mostly confined in the capacitive depletion region but the magnetic field reaches the whole region near the metal lines. Both structures can be designed to have high slow-wave factors of more than 20, where the slow-wave factor is defined by the free-space wavelength (λ_0) divided by the guide wavelength (λ_g).

The direct application of these structures for traveling-wave electrodes has a big obstacle of high losses of the modulation and light waves. The high losses come from the doped-semiconductor substrate which is inherently lossy due to high impurity concentration. The high impurity concentration not only results in high dielectric loss of the modulation wave but also free carrier absorption of the light wave. Therefore, it is fundamental to use a slow-wave electrode based on a semi-insulating GaAs substrate

for the traveling-wave optical modulator. The slow-wave structure used in this research[13],[14] is a certain construction of metal and insulator based on a semi-insulating GaAs substrate. Therefore, the dielectric loss as well as the free carrier loss can be avoided but the conductor loss is predominant and even higher than in normal structures.

2.2. Physics of the periodic slow-wave structure

The essential task of energy separation for a slow-wave structure has been performed in the cross-sectional direction for the MIS and Schottky slow-wave structures. In this cross-tie slow-wave structure, the electric and magnetic energies are periodically separated in the longitudinal direction of propagation. Fig.2.1(a) shows the schematic diagram of the longitudinal separation of the energies which is an infinitely periodic array of two quite different line sections A and B. If we can store the electric and magnetic energies into sections A and B, respectively, this periodic energy separation can result in a slow-wave phenomenon and then, electromagnetic waves can travel slowly in this structure. Here, the two section lengths (l_A and l_B) must be much shorter than the guide wavelength in order to keep the fields of adjacent sections in phase. Otherwise, the electric and magnetic energies cannot be separated effectively. Actually, if one period length of the array is much shorter than the guide wavelength, this structure behaves as a uniform transmission line macroscopically and has inherently wideband characteristics. On the other hand, if the period is comparable to the guide wavelength, this structure behaves as a Bragg reflector and the wideband characteristic will be lost.
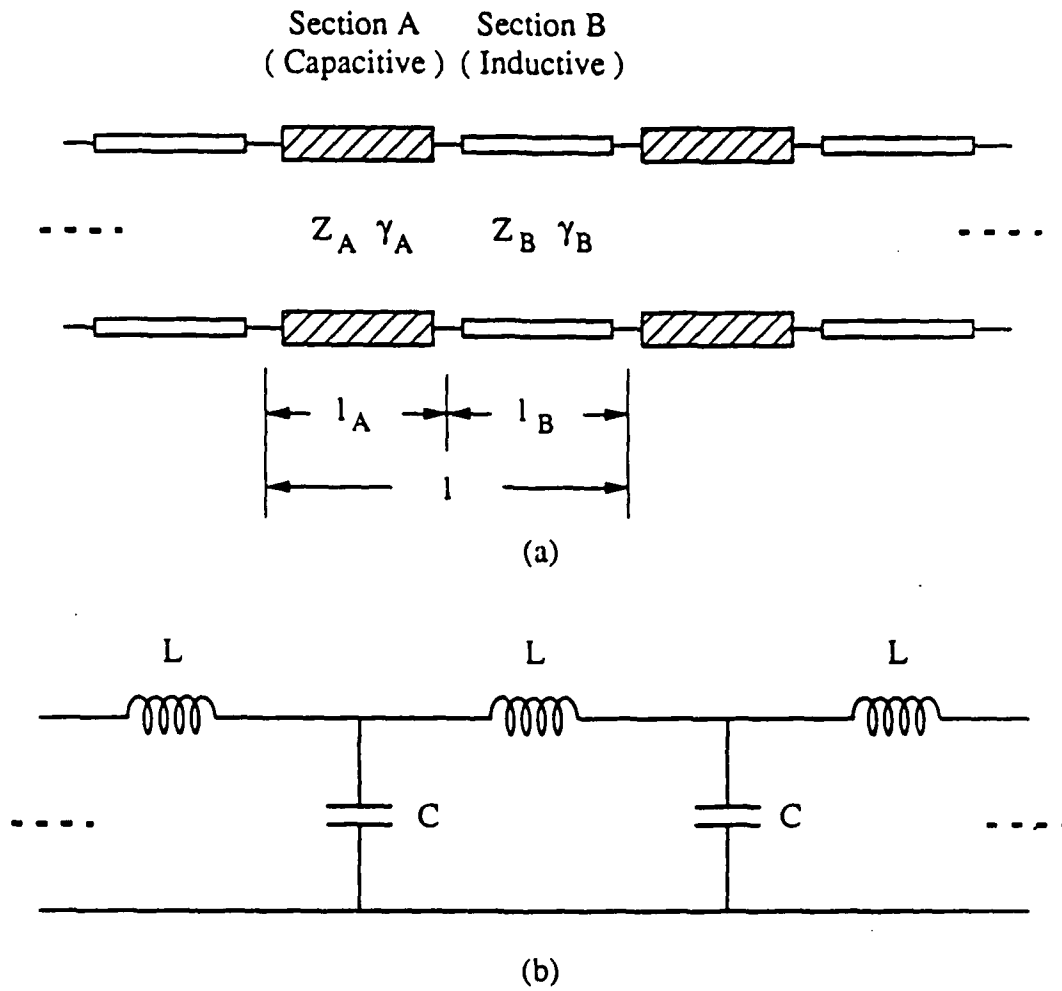
Fig. 2. 1. (a) Periodic seperation of electrical and magnetic energies into

two different transmission line sections and (b) Equivalent

circuit of an ideal transmission line

It is obvious that the electric and magnetic energies can be stored effectively in a capacitor and an inductor, respectively. Therefore, section A and section B must be capacitive and inductive, respectively, or vice versa, in order to separate the energies. In an extreme case, section A and section B become pure capacitor and inductor, respectively. That is the case of an ideal transmission line shown in Fig.2.1(b) where the electric and magnetic energies are completely separated into a capacitor and an inductor. Here, a fundamental difference between the slow-wave structure and normal transmission lines is that the capacitance and the inductance can be changed individually in the slow-wave structure using the periodic sections but not in normal transmission lines due to the energy coupling.

2.3. Realizations of the periodic slow-wave structure and the periodic cross-tie overlays

In order to realize the slow-wave structure, a normal transmission line can be periodically loaded with lumped capacitors of high capacitance as shown in Fig.2.2(a). However, the method is not appropriate for small device as well as monolithic integration. Instead of using the lumped capacitor, geometrical dimensions of normal transmission lines can be regularly modulated in order to change the line capacitances periodically as shown in Fig.2.2.(b)-(d) where the strip conductors of microstrip, coplanar waveguide, and coplanar strip are periodically modulated.

The method of changing geometrical dimensions is not adequate to get high slow-wave factors because the effect sometimes will saturate due to the excess modulation of geometrical dimension. More general and effective way to make a slow-
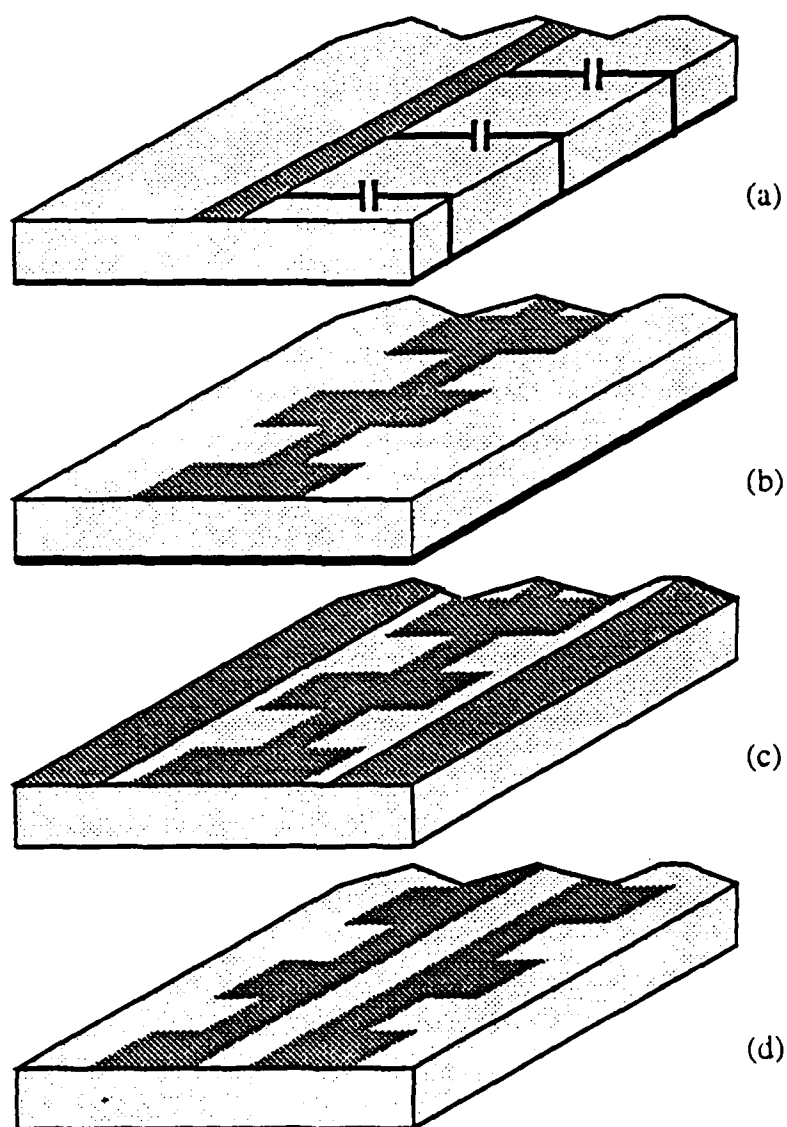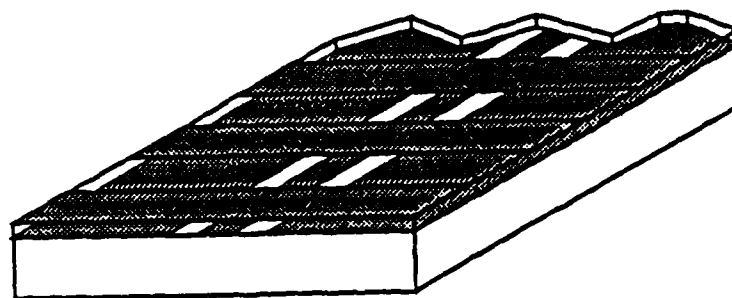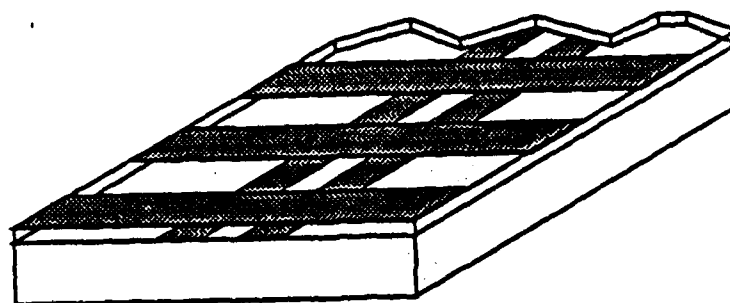
Fig. 2. 2. Periodic slow-wave structures using (a) Periodic capacitor
loading, Geometry modulations of (b) Microstrip, (c) Coplanar
waveguide, and (d) Coplanar strip

(a)

(b)

Fig. 2. 3. Slow-wave structures using periodic cross-tie metal

overlays on (a) Coplanar waveguide and (b) Coplanar strip

wave structure is to add another layer of periodic metal overlays on top of the normal strip lines as shown Fig.2.3. This method is especially suitable for coplanar lines because high periodic capacitance can be easily obtained using the metal overlays. The metal overlays are not necessary to be electrically connected to the metal strips since the high periodic capacitance is obtained between the metal strips and the metal overlays.

2.4. Analysis of the periodic slow-wave structure using Floguet's theorem

Periodic slow-wave structures shown in the previous section are a periodic array of one unit cell consisted of a capacitive section A and an inductive section B. The unit cell can be represented by the transfer matrix of two-port network. If we know the transfer matrix, we can directly apply Floquet's theorem to the periodic array and obtain the overall transmission characteristics of the slow-wave structure.

The unit cell with finite length ($l=l_A+l_B$) can be analyzed using a full-wave analysis to obtain the accurate transfer matrix. However, because of complexity of the full-wave analysis, we use a transmission line approach to obtain the transfer matrix. This approach represents each section as a transmission line with a complex propagation constant (γ) and a characteristic impedance (Z). Therefore, for a given finite section ($l = l_A$ or l_B) of the transmission line, the transfer matrix can be obtained simply as follows.

$$\begin{bmatrix} A & B \\ C & D \end{bmatrix} = \begin{bmatrix} \cosh \gamma l & Z \sinh \gamma l \\ \dfrac{1}{Z} \sinh \gamma l & \cosh \gamma l \end{bmatrix} \tag{2.1}$$

Since voltage and current must be continuous at each junction between section A and section B, transfer matrix of the unit cell can be obtained by multiplying the transfer matrices of the two sections. Therefore,

$$
\begin{bmatrix} A & B \\ C & D \end{bmatrix}_{Unit\,cell} = \begin{bmatrix} A & B \\ C & D \end{bmatrix}_{Section\,A} \begin{bmatrix} A & B \\ C & D \end{bmatrix}_{Section\,B}
$$

$$
= \begin{bmatrix} \cosh \Psi_A & Z_A \sinh \Psi_A \\ \dfrac{1}{Z_A} \sinh \Psi_A & \cosh \Psi_A \end{bmatrix} \begin{bmatrix} \cosh \Psi_B & Z_B \sinh \Psi_B \\ \dfrac{1}{Z_B} \sinh \Psi_B & \cosh \Psi_B \end{bmatrix}
$$

$$
= \begin{bmatrix} \cosh\Psi_A \cosh\Psi_B + \dfrac{Z_A}{Z_B}\sinh\Psi_A\sinh\Psi_B & Z_B\cosh\Psi_A\sinh\Psi_B + Z_A\sinh\Psi_A\cosh\Psi_B \\ \dfrac{1}{Z_A}\sinh\Psi_A\cosh\Psi_B + \dfrac{1}{Z_B}\cosh\Psi_A\sinh\Psi_B & \dfrac{Z_B}{Z_A}\sinh\Psi_A\sinh\Psi_B + \cosh\Psi_A\cosh\Psi_B \end{bmatrix}
$$

$$(2.2)$$

where Ψ_A and Ψ_B are respectively defined by $\gamma_A l_A$ and $\gamma_B l_B$ for simplicity. This approach is reasonable since each section is just a transmission line with finite propagation length and shows good agreement with full-wave analysis[15]. Some deviation is expected due to discontinuity effects at each junction. The main discontinuity effect is the stray capacitance at each junction and this additional capacitance enhances the slow-wave factor.

Floquet's theorem[16] states: For a given mode of propagation at a given frequency in a periodic array, fields at one cross-section differ from those a period away only by a complex constant. The theorem is true for any periodic structure with or without loss. It is obvious that one-period displacement of an infinite array in the axial direction does not make any difference to the original structure. Therefore, if a

propagating mode is supported by a periodic array, the field in (n+1)th period can be mathematically expressed as that in nth period delayed by a complex propagation constant (γ) of the mode. The complex constant ($\gamma = \alpha + j\beta$) consists of the attenuation constant (α) and the phase constant (β). This relation is written for the voltages and currents on the two concatenated nodes of the periodic array as follows.

$$\begin{bmatrix} V_{n+1} \\ I_{n+1} \end{bmatrix} = e^{-\gamma l} \begin{bmatrix} V_n \\ I_n \end{bmatrix} \tag{2.3}$$

where $l \,(= l_A + l_B)$ is total length of one unit cell. Using (2.2) and (2.3), we can get an eigenvalue equation for the complex propagation constant (γ) of the guided mode.

$$\left(\begin{bmatrix} A & B \\ C & D \end{bmatrix}_{\text{Unit cell}} - e^{-\gamma(l_A + l_B)} \right) \begin{bmatrix} V_n \\ I_n \end{bmatrix} = 0 \tag{2.4}$$

Non-trivial solution of the eigenvalue equation (2.4) gives us the complex propagation constant (γ) of the periodic array as a function of the complex propagation constants (γ_A, γ_B), the characteristic impedances (Z_A, Z_B), and section lengths (l_A, l_B) of the two sections. The dispersion equation obtained is

$$\cosh \gamma l = \cosh \gamma_A l_A \cosh \gamma_B l_B + \frac{1}{2}\left(\frac{Z_A}{Z_B} + \frac{Z_B}{Z_A}\right) \sinh \gamma_A l_A \sinh \gamma_B l_B \tag{2.5}$$

Characteristic impedance (Z_0) of the array can be obtained from the voltage and the current at a node which are determined from the eigenvector of (2.4).

$$Z_0 = \sqrt{\frac{Z_B \cosh\gamma_A l_A \sinh\gamma_B l_B + Z_A \sinh\gamma_A l_A \cosh\gamma_B l_B}{\frac{1}{Z_A} \sinh \gamma_A l_A \cosh\gamma_B l_B + \frac{1}{Z_B} \cosh\gamma_A l_A \sinh\gamma_B l_B}} \tag{2.6}$$

Here, the section lengths (l_A, l_B) are short enough to keep the adjacent sections in phase and both phase constants (β_A, β_B) are very close to each other in many cases. And characteristic impedance of capacitive section A is much smaller than that of inductive

section B to obtain the high slow-wave factor. Therefore, the parameters in (2.5) and (2.6) are in general within some ranges, in which $|\gamma_A l_A|$, $|\gamma_B l_B| \ll 1$, $\beta_A \approx \beta_B$, and $|Z_A| \ll |Z_B|$. In these typical ranges of parameters, the equations (2.5) and (2.6) can be reduced to the following simple expressions which can visualize the slow-wave phenomenon.

$$\beta \approx \beta_A \sqrt{\frac{1 + T K + T^2}{(1 + T)^2}} \qquad (2.7)$$

$$\alpha \approx \left(\frac{\beta_A}{\beta}\right) \left[\frac{\alpha_A + T^2 \alpha_B + \frac{K T}{2}(\alpha_A + \alpha_B)}{(1 + T)^2}\right] \qquad (2.8)$$

$$Z_0 \approx \sqrt{Z_A Z_B \left(\frac{T K}{K + T}\right)} \qquad (2.9)$$

where $K = |Z_B/Z_A|$ and $T = l_B/l_A$.

If we look at the equation (2.7), we can find β higher than β_A since $1 \ll K$ for any T. This means a periodic array of high and low characteristic impedances, associated with capacitive and inductive sections respectively, has inherently slow-wave property, i.e. lower phase velocity than the individual section. On the other hand, total attenuation of the slow-wave structure in (2.8) is increased from average attenuation of two sections approximately by a factor of β/β_A in the case of T=1. This is because a slow-wave takes more time and travels longer distance to pass through a finite length of a slow-wave structure due to the slower phase velocity.

In the event of $1 \ll K$ and $l_A \approx l_B$, β and Z_0 in (2.7) and (2.9) are approximately proportional to $(Z_B/Z_A)^{1/2}$ and $(Z_A Z_B)^{1/2}$, respectively and hence, we can easily reduce the phase velocity of the slow-wave structure while maintaining a given characteristic impedance. Therefore, this property can be applied very effectively to achieve simultaneous matching of the phase velocities and the characteristic impedance of traveling-wave optical modulators. Furthermore, since this slow-wave structure is almost dispersionless due to the uniform transmission line behavior, it is especially suitable for wideband traveling-wave optical modulators. Next two chapters describe two wideband GaAs traveling-wave optical modulators using the cross-tie slow-wave structures based on coplanar strip and coplanar waveguide electrodes.

GaAs Traveling-wave Optical Modulator using a Modulated Coplanar Strip Electrode with Periodic Cross-tie Overlays
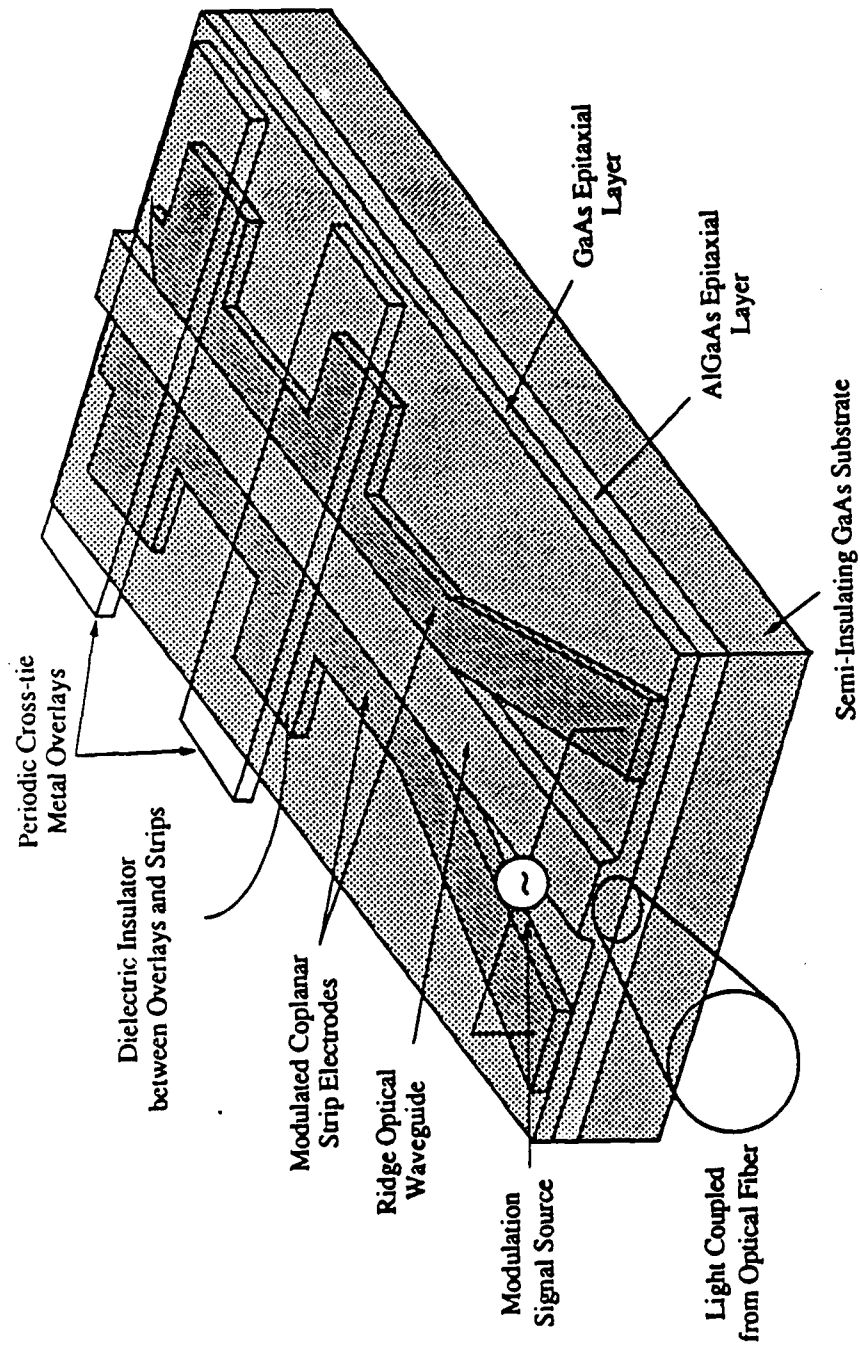
3.1. Introduction

The previous chapter described a cross-tie slow-wave structure which has good potential of wideband velocity matching of modulation and optical waves in traveling-wave optical modulators. The slow-wave structure reduces the phase velocity of the modulation wave and can be designed to match the phase velocities and the characteristic impedance simultaneously. In this chapter, described is a GaAs traveling-wave optical modulator using a modulated coplanar strip electrode with periodic cross-tie overlay[17],[18]. All GaAs traveling-wave optical modulators using conventional coplanar electrodes have an eventual limitation of bandwidth due to the phase velocity mismatch. In this novel structure, the cross-tie slow-wave structure is applied to a GaAs traveling-wave optical modulator based on a modulated coplanar strip electrode and then, the phase velocities and the characteristic impedance are matched successfully in order to maximize the bandwidth. The width of the coplanar strip electrode is periodically modulated to reduce the dominant conductor loss while keeping both matching conditions of the phase velocities and the characteristic impedance at high frequencies. The calculated 3-dB bandwidth and modulation voltage are 100 GHz and 23 V, respectively, for 4-mm-long modulator at 1.3-μm light wavelength. And the

modulation characteristic varies slowly over the bandwidth because the phase velocity matching is satisfied. The slow-wave structure has been build on a semi-insulating GaAs substrate and measured using a microwave network analyzer. The measured phase velocity is much lower than that of conventional coplanar-electrodes and agrees very well with the calculated one.
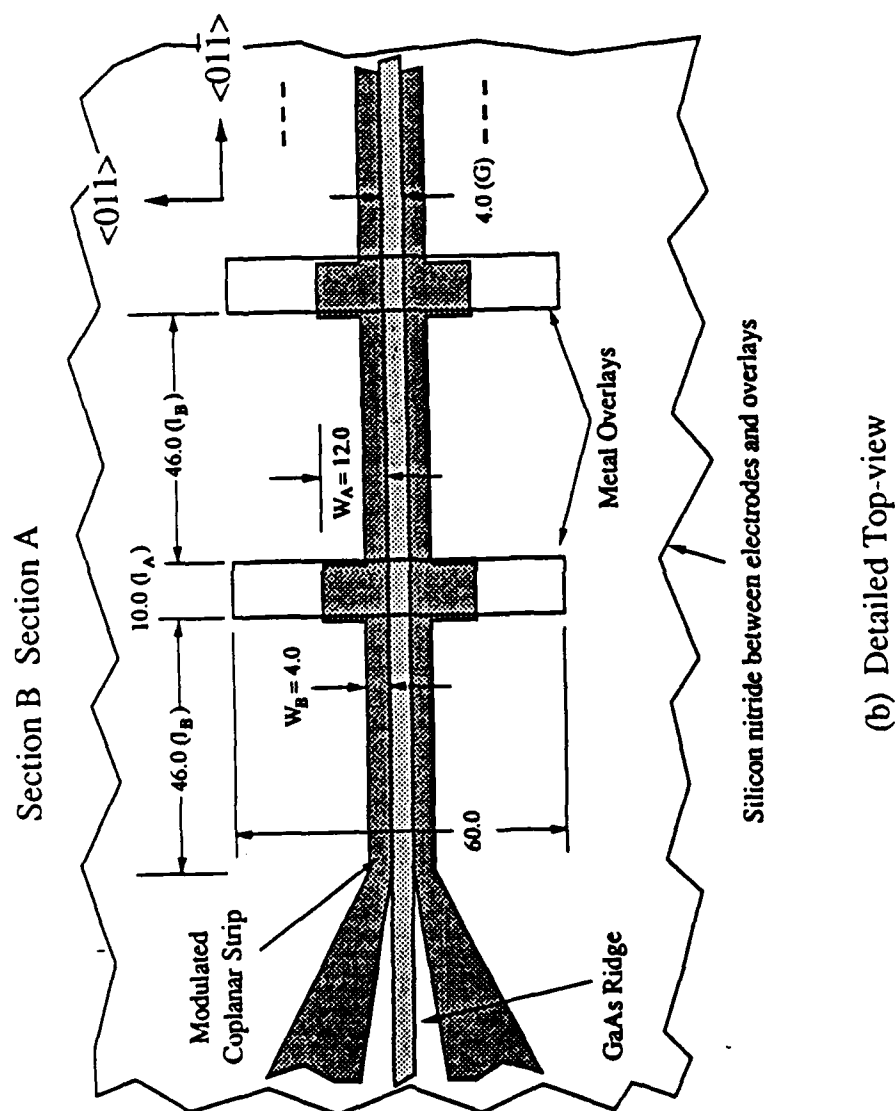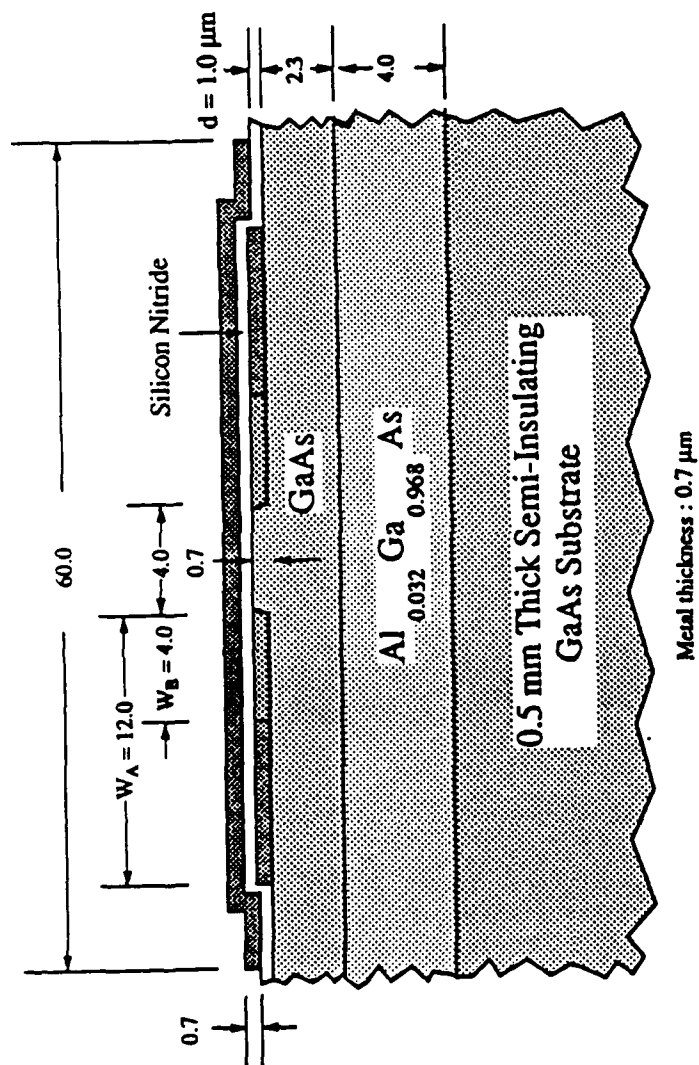
3.2. Structure description

The GaAs traveling-wave optical modulator shown in Fig.3.1 is constructed with a coplanar strip slow-wave electrode and a GaAs ridge optical waveguide on a semi-insulating GaAs substrate ($\varepsilon_r = 12.9$). The slow-wave electrode consists of an infinite array of a more capacitive section A (with overlay) and a more inductive section B (without overlay) based on a modulated coplanar strip. Since the period chosen is much smaller than the propagation wavelength, this structure behaves as a uniform transmission line. In this structure, we can increase the effective capacitance (C) and inductance (L) of this transmission line independently by a spatial separation of electric and magnetic energies into the two different sections. Therefore, the phase velocity, which is inversely proportional to $(LC)^{1/2}$, can be decreased below that of common coplanar strip.

In order to reduce the dominant conductor loss, the strip width is periodically modulated because the wider strip of section A results in lower conductor loss to obtain a high capacitance for a given strip gap. The electrode thickness is fixed to the height (=0.7 μm) of the ridge optical waveguide to make the surface flat and the fabrication easy while thicker electrode is better to reduce the high conductor loss at low frequencies. A 1-μm silicon nitride layer ($\varepsilon_r = 6.8$) is deposited onto the strip in order

21

Periodic Cross-tie
Metal Overlays

Dielectric Insulator
between Overlays and Strips

Modulated Coplanar
Strip Electrodes

Ridge Optical
Waveguide

Modulation
Signal Source

Light Coupled
from Optical Fiber

GaAs Epitaxial
Layer

AlGaAs Epitaxial
Layer

Semi-Insulating GaAs Substrate

(a) Overview

(b) Detailed Top-view

Fig. 3. 1. GaAs traveling-wave optical modulator using a modulated coplanar strip with periodic cross-tie overlays

(c) $(01\bar{1})$ Face Cross-Section

Metal thickness : 0.7 μm

0.5 mm Thick Semi-Insulating GaAs Substrate

$Al_{.0032} Ga_{.968} As$

GaAs

Silicon Nitride

$d = 1.0$ μm

2.3

4.0

60.0

$W_A = 12.0$

$W_B = 4.0$

4.0

0.7

0.7

0.7

to insulate the cross-tie overlays from the strip electrode. The both ends of the slow-wave electrode are extended and connected to coaxial lines through intermediate microstrip lines for wideband feeding and termination which will be described in next chapter.

Since this electrode has high DC-resistance (60 Ω) due to the small cross-section, the characteristic impedance is very high at low frequencies as shown in Fig.3.9. Therefore, the electrode is terminated using a 50-Ω resistor in series with a capacitor (6.4 pF) for the matched termination. The termination has high termination impedance at low frequencies which prevents voltage drop in the electrode and improve the DC modulation voltage.

The GaAs ridge optical waveguide can be readily formed on 0.5mm thick (100) semi-insulating GaAs substrate (n = 3.41 at 1.3 μm) using epitaxial growing and mesa etching techniques[19]. Optical and modulation waves propagate along <011> direction and the modulation electric field is in <01$\bar{1}$> direction to use the highest electro-optic effect ($n^3 r_{41} \approx 5.6 \times 10^{-11}$ m/V at 1.3 μm).

3.3. Analysis and optimum design

Numerical analysis of the slow-wave electrode has been carried out by quasi-static analysis[20] and conductor loss calculation for each section, and then by an application of the Floquet's theorem to the periodic array. Since the electrode dimensions are much smaller than the propagation wavelength, the quasi-static analysis for the calculations of the distributed capacitance (C) and inductance (L) is valid and the overall dispersion mainly comes from the high conductor loss and the dispersion of the

periodic array. In the quasi-static analysis, the GaAs regions are assumed to have a uniform dielectric constant ($\varepsilon_r=13.0$) because a slight refractive index difference (~0.02) between the epitaxial layers is high enough to form a single mode propagation of the ridge optical waveguide. The depletion regions to be formed at the electrode-GaAs Schottky junctions as well as the dielectric loss are also neglected in the calculation since the background carrier concentrations of MBE or OMVPE-grown GaAs epitaxial layers are much less than $10^{14}/cm^3$[19].

The dominant conductor losses of the two sections are calculated in wide ranges of frequency and field penetration into the conductor using the phenomenological loss equivalence method[44]-[46]. In this method, a quasi-TEM transmission line, having a finite conductor thickness comparable to the skin depth, is approximated with an equivalent single strip which has the same geometrical factor and DC resistance as the original transmission line. Therefore, the distributed internal impedance has been calculated from the equivalent single strip in the wide range of field penetration and then, all the transmission characteristics are obtained from the equivalent circuit.

The GaAs ridge optical waveguide is designed for a single TE_0-like mode propagation at 1.3-μm wavelength using the effective index-method[21]. In the calculation, the GaAs region is horizontally divided into three planar waveguides of a center ridge and two side clads. The electrode is neglected in the calculation because the optical mode decays very fast in the electrode regions. The calculated horizontal and vertical mode sizes are 4.6 and 2.1 μm, respectively, at 1.3-μm wavelength that are suitable for good coupling to single mode fibers. Since the mode is not intrinsically

leaky, the optical propagation loss, which is mostly imperfection loss, will be very small compared to the high insertion loss predominated by the coupling loss.

3.3.1. Optimum orientation of the GaAs substrate

In order to maximize the electro-optic modulation of GaAs crystal, the GaAs substrate must be properly oriented to the electric field of the modulation wave. The electric field direction of the modulation wave lies almost in horizontal direction within the GaAs ridge waveguide region and in vertical direction just beneath the strip conductors. Since most of the optical mode is confined in the GaAs ridge waveguide, we use the horizontal electric field to modulate the refractive index of the GaAs ridge waveguide. Therefore, the best alignment can be achieved by properly aligning the crystal orientation to the horizontal electric field using the Jones calculus[22]. Here, the best crystal orientation must be chosen in conjunction with the application in order to optimize the device performance in practical situation. This device can be used for amplitude, polarization, and phase modulations of light wave in wide range of frequency. One of the main applications is the phase modulation of light wave for very wideband heterodyne optical communication.

In the application of the phase modulation, there are several conditions for optimum orientation listed below.

(a) the largest electro-optic coefficient to reduce modulation voltage

(b) lightwave propagation perpendicular to the electric field direction for long modulator length

(c) lightwave propagation along a principal axis for temperature and strain stabilities

(d) lightwave polarization along a principal axis for small polarization modulation

All the conditions above cannot be satisfied simultaneously in the case of GaAs substrate. The first two conditions (a) and (b) are more important for low modulation voltage and wide bandwidth while the conditions (c) and (d) should be considered for practical situations.

In order to choose the optimum orientation of the GaAs substrate, we start from the electro-optic tensor (r_{ij}) of GaAs cubic crystal which has $\overline{4}3m$ crystal symmetry in standard crystallographic system as follow[23].

$$r_{ij} = \begin{pmatrix} 0 & 0 & 0 \\ 0 & 0 & 0 \\ 0 & 0 & 0 \\ r_{41} & 0 & 0 \\ 0 & r_{41} & 0 \\ 0 & 0 & r_{41} \end{pmatrix} \tag{3.1}$$

For an applied electric field with E_x, E_y, and E_z components shown in Fig.3.2, the perturbation tensor of impermeability ($\Delta\overline{b}$) in standard crystallographic system then becomes

$$\Delta\overline{b} = \begin{pmatrix} 0 & 0 & 0 \\ 0 & 0 & 0 \\ 0 & 0 & 0 \\ r_{41} & 0 & 0 \\ 0 & r_{41} & 0 \\ 0 & 0 & r_{41} \end{pmatrix} \begin{pmatrix} E_x \\ E_y \\ E_z \end{pmatrix} => \begin{pmatrix} 0 & r_{41}E_z & r_{41}E_y \\ r_{41}E_z & 0 & r_{41}E_x \\ r_{41}E_y & r_{41}E_x & 0 \end{pmatrix} \tag{3.2}$$

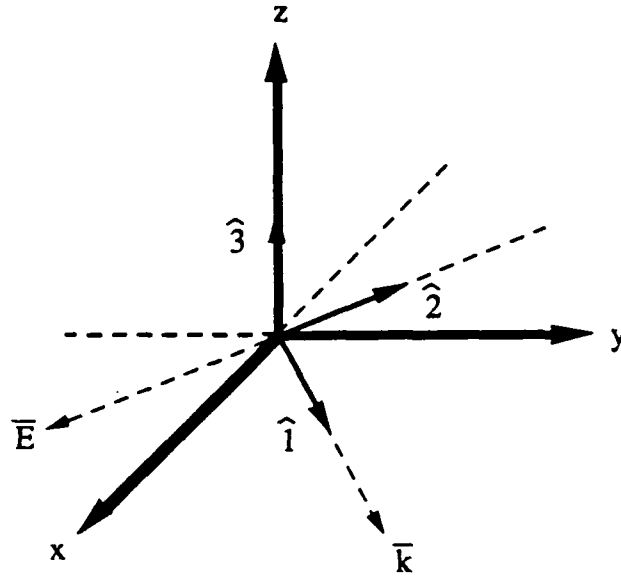
Fig. 3. 2. Standard crystallographic coordinate system (x,y,z)

and the transformed coordinate systems (1,2,3)

Since GaAs is a cubic crystal, the unperturbed impermeability tensor $(\bar{\bar{b}}^{(0)})$ is diagonal and hence, the total perturbed impermeability tensor $(\bar{\bar{b}})$ may be written as

$$\bar{\bar{b}} = \bar{\bar{b}}^{(0)} + \Delta\bar{\bar{b}} = \begin{pmatrix} b_0 & 0 & 0 \\ 0 & b_0 & 0 \\ 0 & 0 & b_0 \end{pmatrix} + \begin{pmatrix} 0 & r_{41}E_z & r_{41}E_y \\ r_{41}E_z & 0 & r_{41}E_x \\ r_{41}E_y & r_{41}E_x & 0 \end{pmatrix} = \begin{pmatrix} b_0 & r_{41}E_z & r_{41}E_y \\ r_{41}E_z & b_0 & r_{41}E_x \\ r_{41}E_y & r_{41}E_x & b_0 \end{pmatrix} \quad (3.3)$$

Now, we choose a propagation direction of optical wave $(\bar{k})$ in parallel to $(\hat{x} + \hat{y})$ direction which will be shown later to be optimum direction of propagation. Instead of working in the principal axis system used previously, we choose a transformed coordinate system (1,2,3) with one axis (1-axis) in the propagation direction of optical wave $(\bar{k})$ as shown in Fig.3.2. The others (2-axis and 3-axis) are in $(-\hat{x} + \hat{y})$ and $(\hat{z})$ directions, respectively. Therefore, the new coordinate system can be

obtained by rotating z-axis of the principal axis system 45^0 counterclockwise. The rotation matrix (T) for the coordinate transform and the perturbed impermeability tensor ($\overline{\overline{b}}\,'$) obtained in the new coordinate system become then

$$T = \begin{pmatrix} \dfrac{1}{\sqrt{2}} & \dfrac{1}{\sqrt{2}} & 0 \\[2mm] -\dfrac{1}{\sqrt{2}} & \dfrac{1}{\sqrt{2}} & 0 \\[2mm] 0 & 0 & 1 \end{pmatrix} \tag{3.4}$$

$$\overline{\overline{b}}\,' = T\,\overline{\overline{b}}\,T^{-1} = \begin{pmatrix} b_0 + r_{41}E_z & 0 & \dfrac{r_{41}}{\sqrt{2}}\,(E_x + E_y) \\[3mm] 0 & b_0 - r_{41}E_z & \dfrac{r_{41}}{\sqrt{2}}\,(E_x - E_y) \\[3mm] \dfrac{r_{41}}{\sqrt{2}}\,(E_x + E_y) & \dfrac{r_{41}}{\sqrt{2}}\,(E_x - E_y) & b_0 \end{pmatrix} \tag{3.5}$$

In the new coordinate system, the dielectric displacement vector ($\overline{D}$) of the optical wave is orthogonal to the wave vector ($\overline{k}$). Therefore, we can neglect the row and column corresponding to the direction of wave vector ($\hat{1}$) and then, get a 2x2 subtensor ($\overline{\overline{b}}\,'_{\perp}$) of the perturbed impermeability tensor as follows.

$$\overline{\overline{b}}\,'_{\perp} = \begin{pmatrix} b_0 - r_{41}E_z & \dfrac{r_{41}}{\sqrt{2}}\,(E_x - E_y) \\[3mm] \dfrac{r_{41}}{\sqrt{2}}\,(E_x - E_y) & b_0 \end{pmatrix} \tag{3.6}$$

If we apply E_z-component only, light polarized at -45^0 in the x-y plane will have the refractive index perturbed by the electric field. For an applied electric field (E) in the direction of ($\hat{x} - \hat{y}$), both orthogonal polarizations perpendicular to the wave vector ($\hat{k} = \hat{x} + \hat{y}$) will be perturbed. If a refractive index for one polarization is increased by the perturbation, the other refractive index for the orthogonal polarization will be reduced. Therefore, the latter case is preferable for higher induced birefringence

between the two waves. In the case of an applied electric field (E) which is in the direction of $(\hat{x} - \hat{y})$, we can solve the eigenvector problem

$$\left(\overline{\overline{b}}_{\perp}' - \lambda \right) \overline{D}_{\perp} = 0$$

yielding eigenvalues and eigenvectors in the new coordinate system ($\hat{2}$-$\hat{3}$ plane) of

$$\text{dir} \left(\overline{D}_1 \right) = \begin{bmatrix} 1 \\ 1 \end{bmatrix}_{\lambda_1 = b_0 + r_{41} E} \quad \text{and} \quad \text{dir} \left(\overline{D}_2 \right) = \begin{bmatrix} 1 \\ -1 \end{bmatrix}_{\lambda_2 = b_0 - r_{41} E}$$
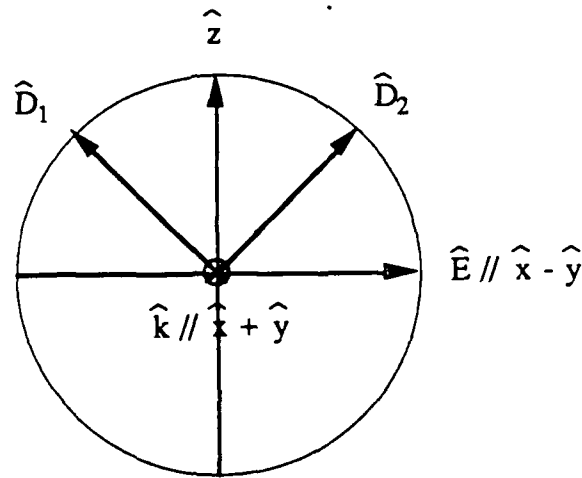

Fig. 3. 3. Two orthogonal polarizations (D_1 and D_2) induced

by the applied electric field (E)

In the standard coordinate system shown in Fig.3.3, D_1 and D_2 are in $(-\hat{x}+\hat{y}+\hat{z})$ and $(\hat{x}-\hat{y}+\hat{z})$ directions, respectively, with the propagation direction of $(\hat{k} = \hat{x} + \hat{y})$. From the eigenvalues of the impermeability tensor, we can obtain the perturbed refractive indices for the two orthogonal polarizations as follow.

$$n_{1, 2} = \frac{1}{\sqrt{\lambda_{1, 2}}} \approx n_0 \pm \frac{n_0^3}{2} r_{41} E \qquad (3.7)$$

where n_0 is the unperturbed refractive index of GaAs crystal and the last perturbation term is much smaller than n_0.

The optimum orientation of GaAs substrate shown in Fig.3.1. has been realized using (100) face GaAs substrate because (100) surface of GaAs substrate has better quality of epitaxial growing. In the GaAs substrate, the ridge optical waveguide lies in $<01\bar{1}>$ direction and the electric field of modulation wave is applied in $<0\bar{1}\bar{1}>$ direction using the coplanar strip electrode.

3.3.2. Quasi-static analysis of the coplanar strip slow-wave electrode

Each section of the slow-wave electrode has been analyzed using quasi-static analysis and the phenomenological loss equivalence method which calculate the distributed capacitance and inductance, and the internal impedance due to field penetration, respectively. The calculated elements are then incorporated into the circuit model of the transmission line to obtain the complex propagation constants and characteristic impedances of the two sections. Finally, overall complex propagation constant and characteristic impedance of the slow-wave electrode have been calculated by inserting the complex propagation constants and characteristic impedances of the two sections into the Floquet equations (2.5) and (2.6). The quasi-static analysis is valid in this periodic array since most of dispersion comes from the periodic array and is included in the Floquet equations (2.5) and (2.6). The GaAs substrate is assumed to have a uniform dielectric constant because the difference of dielectric constants of AlGaAs and GaAs epitaxial layers is negligible in modulation frequency range. And the substrate is also assumed to be infinite because the coplanar strip is very small compared to the thick substrate. Schottky depletion layers formed beneath the metal

electrodes are also neglected because of very small background carrier concentration of GaAs epitaxial layer grown in MBE. The slightly depleted layers are expected to enhance the slow-wave phenomenon a little.

In the quasi-static analysis[20], the propagating mode of a quasi-TEM transmission line is assumed to be pure TEM. This means that if we replace all the dielectric materials by air, the phase velocity will be the free-space phase velocity (c) and then, the effective distributed inductance ($L=1/c^2 C^a$) can be calculated from the air capacitance (C^a). This inductance will be the actual inductance of the original line with dielectric materials since the dielectric materials do not affect the magnetic flux and hence, the inductance. Using transmission line analogy, the characteristic impedance and the effective index of the lossless transmission line can be written in terms of the actual capacitance C and the air capacitance C^a as follow.

$$Z_0 = \sqrt{\frac{L}{C}} = \frac{1}{c}\sqrt{\frac{1}{C^a C}} \quad \text{and} \quad \varepsilon_{reff} = c^2 L C = \frac{C}{C^a} \qquad (3.8)$$

This is valid for any quasi-TEM transmission line supporting a quasi-TEM mode such as microstrip, coplanar waveguide, and coplanar strip.

3.3.2.1. Section A

The cross-sectional configuration of section A is shown in Fig.3.4 which consists of two coplanar strip conductors with a metal overlay on a GaAs substrate. Actually, this structure is an inverted coupled microstrip line in which the air region is replaced by the silicon nitride layer. This structure can support two quasi-TEM modes of even and odd symmetry. We, however, consider the odd mode only because the even mode quite differs from the mode of section B and therefore, cannot propagate in

the periodic array. Since this structure is symmetric in horizontal direction, we can put an electric wall in the center and consider one half side for simplicity.
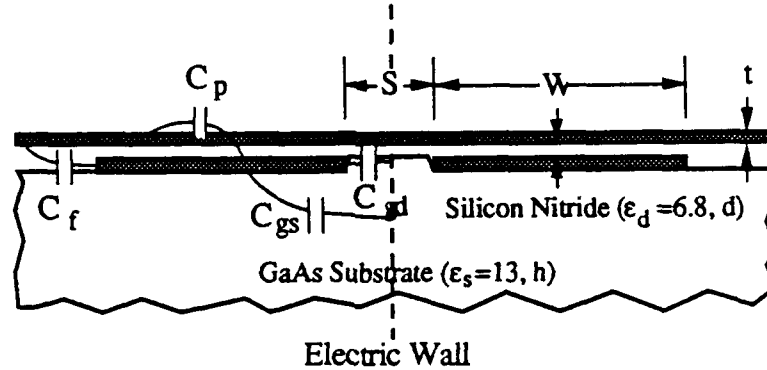

Fig. 3. 4. Cross-section of section A

For the quasi-static analysis, total odd mode capacitance of the half side (C_o) is decomposed into four components as shown in Fig.3.4. C_{gs} and C_{gd} are the capacitances between the coplanar strip and the electric wall through the GaAs substrate and through the dielectric layer of silicon nitride, respectively. C_p is the parallel plate capacitance between the strip and the metal overlay, and, finally, C_f is the fringe capacitance of the coplanar strip. Therefore, the total capacitance (C_o) can be written as

$$C_o = C_p + C_{gs} + C_{gd} + C_f \qquad (3.9)$$

In the four capacitances, the parallel plate capacitance ($C_p = \varepsilon_0 \varepsilon_d W/d$) is predominant because the strip width ($W \sim 12 \mu m$) as well as the strip gap ($S \sim 4 \mu m$) are much larger than the dielectric thickness ($d < 1 \mu m$). Therefore, the fringe capacitance of the strip

(C_f) can be approximately calculated from the fringe capacitance of a microstrip line as follows.

$$C_f = \frac{(C_m - C_p)}{2} = \frac{1}{2}\left(\frac{\sqrt{\varepsilon_{rem}}}{c\,Z_{om}} - \varepsilon_0\,\varepsilon_d\frac{W}{d}\right) \qquad (3.10)$$

where C_m, Z_{om}, and ε_{rem} are the capacitance, the characteristic impedance, and the effective index of the microstrip line and can be readily calculated using empirical formulas[47]. The capacitance (C_{gd}) shown below has been obtained from the capacitance expression for a coupled microstrip line which consists of contributions from the coupled stripline geometry and the fringe effect of microstrip line[20].

$$C_{gd} = \frac{\varepsilon_0\,\varepsilon_d}{\pi}\ln\left[\coth\left(\frac{\pi\,S}{4\,d}\right)\right] + 0.65\,C_f\left[\frac{0.02\,d}{S}\sqrt{\varepsilon_d} + \left(1 - \frac{1}{\varepsilon_d^2}\right)\right] \qquad (3.11)$$

Finally, the substrate capacitance (C_{gs}) can be expressed simply as follows using conformal mapping[24].

$$C_{gs} = \varepsilon_0\,\varepsilon_s\frac{K(k')}{K(k)} \quad \text{and} \quad k = \frac{S}{S + 2\,W} \qquad (3.12)$$

where $K(k)$ and $K(k')$ denote the elliptic function and its complement, respectively.

Now, we replace all the dielectric materials with air and calculate the total capacitance (C_o^a) in the same manner as for C_0. Then, the distributed inductance (L_0) can be obtained from the free-space phase velocity (c) as follows.

$$L_o = \frac{1}{c^2\,C_o^a} \qquad (3.13)$$

Since electromagnetic fields penetrate deep into the thin strip conductor due to the finite conductivity, the internal impedance including distributed resistance (R_0) and

internal inductance (L_i) must be calculated and added into the equivalent circuit in wide frequency range. The internal impedance of section A has been analyzed in a wide range of field penetration using the new phenomenological loss equivalence method (PEM)[44]-[46]. In the method, geometric factor and DC resistance of a quasi-TEM line are used to obtain the geometry of an equivalent single strip which is assumed to have the same internal impedance as the original line. The equivalent strip is then analyzed using the surface impedance of the equivalent strip with a finite thickness.

The geometric factor (G) of section A can be calculated from the total inductance increment (∂L) due to the recessions (∂n) of the conducting walls as follows.

$$G = \frac{1}{\mu} \sum_m \left(\frac{\partial L}{\partial n_m} \right) \approx \frac{\varepsilon_0}{\mu_r} \sum_m \left[\frac{\partial \left(C_o^a \right)^{-1}}{\partial n_m} \right] \qquad (3.14)$$

where μ_r is the relative permeability of the conductor used for the strips. As mentioned previously, the capacitance (C_o^a) can be approximately calculated from the capacitance of a microstrip line since the dielectric thickness is very thin compared to the strip width as well as the gap and then, the parallel capacitance is much dominant. Therefore, the geometric factor (G) can be calculated using the geometric factor of a microstrip line rather than directly calculating the derivative of the C_o^a. The effective cross-section (A) used in the PEM formulation is the cross-section (Wt) of one strip here. Therefore, by inserting the G and A into the PEM formulation, we can calculate the distributed resistance and internal inductance of the half side of section A. In addition, we can also insert a conductance element (G_o) associated with the dielectric loss but it is negligible in this structure compared to the dominant conductor loss associated with the distributed resistance.

Up to now, the calculations of the distributed elements has been described. Now, the propagation characteristics such as the complex propagation constant (γ_0) and the characteristic impedance (Z_{0o}) can be calculated as follow by inserting the element values into the equivalent circuit model.

$$\gamma_0 = \sqrt{\left[R_o + j\omega(L_o + L_i)\right]\left(G_o + j\omega C_o\right)} \qquad (3.15)$$

$$Z_{0o} = \sqrt{\frac{R_o + j\omega(L_o + L_i)}{G_o + j\omega C_o}} \qquad (3.16)$$

The final characteristic impedance (Z_A) and the complex propagation constant (γ_A) of section A can be obtained from the above γ_0 and Z_{0o} of one half side by noting that section A is connected to section B through the two coplanar strip electrodes and voltage and current are continuous at the junction. In section A, total odd mode voltage between the coplanar strips is then twice the voltage between one strip and the metal overlay for a given current flowing in the strips. Consequently, the actual Z_A will be twice the Z_{0o} while the complex propagation constants are the same.

$$\gamma_A = \gamma_0 \quad \text{and} \quad Z_A = 2Z_{0o} \qquad (3.17)$$

3.3.2.2. Section B

Section B shown in Fig.3.5 is a coplanar strip with a thin dielectric overlay on GaAs substrate. In this structure, total capacitance consists of a substrate capacitance (C_{gs}) and a capacitance (C_{da}) in dielectric and air regions. It is obvious that the substrate capacitance is the same as that in section A. The C_{da} however, needs some
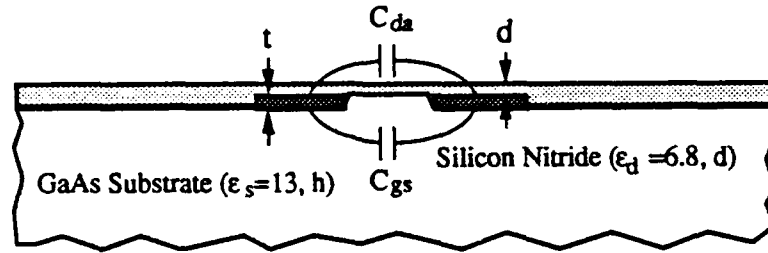
Fig. 3. 5. Cross-section of section B

correction due to the finite dielectric layer. The effect of the thin dielectric layer can be incorporated into the capacitance calculation using the closed form expression of the effective index (ε_{re}) of a coplanar strip with finite substrate thickness[25]. If we define C_a as the capacitance of the coplanar strip filled with air, the capacitance C_{da} then can be expressed by subtracting one half of the air capacitance ($C_a/2$) from the total capacitance ($\varepsilon_{re}C_a$) of the coplanar strip with dielectric layer. Therefore, the capacitance in the dielectric and air region (C_{da}) as well as the total capacitance of section B (C_B) can be expressed simply as follow.

$$C_{da} = \varepsilon_{re} C_a - \frac{C_a}{2} \tag{3.18}$$

$$C_B = C_s + C_{da} = \left[\varepsilon_{re} + \frac{\left(\varepsilon_s - 1 \right)}{2} \right] C_a \tag{3.19}$$

The external inductance (L_B) of section B can be also expressed from the air capacitance of section B as shown in (3.13). The distributed resistance has been calculated by applying the phenomenological loss equivalence method to the coplanar strip. The geometric factor of section B is derived from the empirical formulas[20] and

the effective cross-section used is one half of the cross-section of one strip since the two coplanar strips double the resistance of one strip to make the total resistance at complete field penetration. The complex propagation constant (γ_B) and the characteristic impedance (Z_B) of section B can be obtained by incorporating the distributed elements into the circuit model of the transmission line.

3.3.3. Effective index method for the ridge optical waveguide

The GaAs ridge optical waveguide has been horizontally divided into three constituent regions of a center ridge and two side slab waveguides to apply the effective index method[21] in the horizontal direction as shown in Fig.3.6. Each part is then treated as an asymmetric planar slab waveguide in which the substrate, film, and clad are AlGaAs, GaAs, and dielectric insulator layers, respectively because the optical mode decays very fast in the dielectric layer due to the high index difference between the silicon nitride layer and the GaAs film. The coplanar strip electrodes are neglected in this optical waveguide analysis since the optical field is very small in the electrode regions and Schottky junction is also negligible because of semi-insulating substrate. Some optical field in the electrode regions results in small optical loss due to the metal absorption but it is negligible compared to the dominant coupling loss to optical fiber. In most of semi-insulating GaAs waveguides shorter than 1cm, the waveguide propagation loss including electrode loss, absorption loss, and radiation loss due to the waveguide imperfection is less than 1 dB which is negligible compared to the high coupling loss of about 7-8 dB[19].
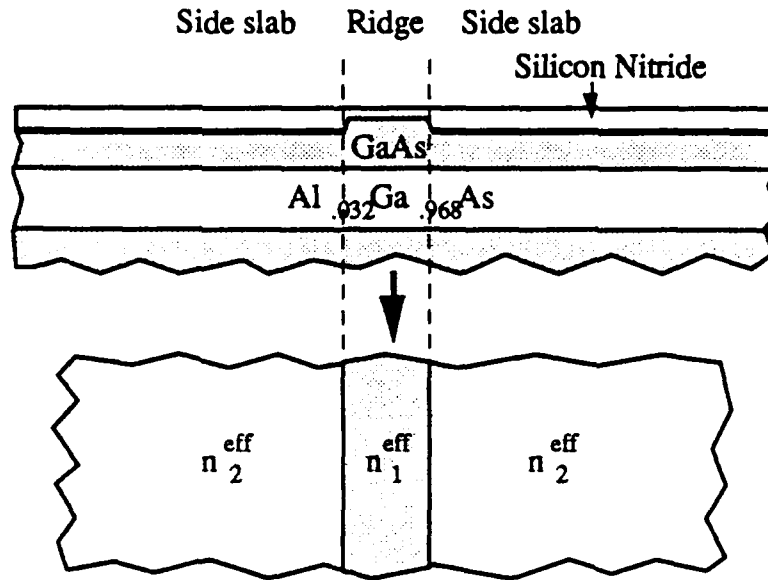
Side slab   Ridge   Side slab

Silicon Nitride

GaAs

Al $_{.932}$Ga $_{.968}$As

n_2^{eff} n_1^{eff} n_2^{eff}

Fig. 3. 6. Cross-section of the ridge waveguide and the equivalent slab waveguide

In the planar slab waveguide, there are two types of mode, TE and TM, traveling with the close dispersion characteristics. Since the ridge waveguide consists of three slab waveguides having different film thickness, two geometrical discontinuities exist at the junctions. Therefore, it is easy to expect that a TE or TM-wave incident on a discontinuous ridge side at an angle, produces not only a reflected and transmitted wave of its own polarization, but also excites a transmitted wave of the other polarization. This TE-TM mode coupling[26] is essential in this kind of discontinuous structure and gives rise to the leakage of the ridge optical waveguide under some circumstances such as for narrow and high ridge. In the case of narrow and high ridge waveguide, if we excite a TM mode inside the ridge, the TM mode can be leaked out through the mode coupling to the TE mode in the side slab waveguides

because the TE-mode can have even larger effective index than the TM mode inside the ridge.

However, since this ridge waveguide has small index difference between GaAs film and AlGaAs substrate, the TE modes is slightly more fundamental than the TM modes and their dispersions are very close to each other. Therefore, in spite of the mode coupling, both modes are inherently well-guided and not leaky for any mode excitation if the ridge is not extremely narrow and high. In addition, the propagation constants of a TE_n and a TM_n mode are almost the same for a wide range of ridge geometry. Therefore, in order to design a leakless single mode ridge waveguide, a fundamental TE_0 mode excitation is assumed at reasonably low ridge height. Due to the mode coupling, the actual mode will be hybrid mode in which predominant field energy is in the TE_0 mode, and hence we characterize the mode as TE_0-like mode.

The effective index of each slab waveguide for the ridge and the side waveguides has been obtained using the mode analysis of planar waveguide[27]. In the analysis, Maxwell's equations have been solved with the boundary conditions of continuous electric and magnetic fields at the two dielectric interfaces. Field variation in the horizontal direction is assumed to be zero as well because infinitely wide slab waveguide is assumed. The dispersion equations for TE and TM modes obtained are written as

$$\tan u = \frac{u\left[\sqrt{v^2 - u^2} + \sqrt{v^2(1 + a_H) - u^2}\right]}{u^2 - \sqrt{(v^2 - u^2)\left[v^2(1 + a_H) - u^2\right]}} \quad \text{for TE modes}$$

$$\tan u = \frac{n_f^2 u\left[n_c^2 \sqrt{v^2 - u^2} + n_s^2 \sqrt{v^2(1 + a_H) - u^2}\right]}{n_c^2 n_s^2 u^2 - n_f^2 \sqrt{(v^2 - u^2)\left[v^2(1 + a_H) - u^2\right]}} \quad \text{for TM modes}$$

$$u = h \sqrt{k^2 n_f^2 - \beta^2} \quad \text{and} \quad v = k h \sqrt{n_f^2 - n_s^2}$$

$$a_H \equiv \frac{n_s^2 - n_c^2}{n_f^2 - n_s^2} \qquad (3.20)$$

where k and h are the free space wavevector and the film thickness. The cutoff

frequencies (v_{cn}) can be obtained from the condition of u = v. Then,

$$v_{cn} = \tan^{-1} \sqrt{a_H} + n \pi \quad \text{for } TE_n \text{ modes}$$

$$= \tan^{-1} \frac{n_f^2}{n_c^2} \sqrt{a_H} + n \pi \quad \text{for } TM_n \text{ modes} \qquad (3.21)$$

The effective indices of the two slab waveguides corresponding to the ridge and the

side slab waveguides are obtained. Now, we replace the ridge and the side slab

waveguides with the dielectric materials of corresponding effective indices to make the

equivalent single slab waveguide as shown in Fig.3.6. Then we apply the same

analysis for the equivalent vertical slab waveguide in which the thickness and the

refractive index of the equivalent film is the width and the effective index of the ridge.

There are many possible combinations of the waveguide geometry and the

refractive indices to make a single mode propagation. In order to reduce radiation loss

due to waveguide imperfection and the mode coupling, normalized frequency (v) must

be far above the cutoff frequency of the fundamental mode in the equivalent slab. On

the other hand, in order to suppress the higher modes, the normalized frequency must

be below the cutoff frequencies of the higher modes. Since optical modulators usually

use short waveguides, higher mode generation inside the waveguide is not importance

and hence we can put the normalized frequency at the cutoff frequency (v_{c1}) of second

mode. Here, wide and low ridge waveguide and reasonably small index difference are

preferable for small loss and easy fabrication for the cutoff frequency (v_{c1}). The geometry and the refractive index of the ridge waveguide shown in Fig.3.1 have been calculated based on these design considerations.

3.3.4. Overlap integral between applied electric field and optical mode

Since the applied electric field and the optical field are not uniform in the GaAs region, the index change induced by the applied voltage (V) must be integrated throughout the GaAs region as follows.

$$\overline{\Delta n} (V) = -\frac{n^3 r}{2} \int_{GaAs\ region} E|E'|^2 dA = -\frac{n^3 r}{2} \frac{V}{G} \Gamma \qquad (3.22)$$

$$\Gamma \equiv \frac{G}{V} \int_{GaAs\ region} E|E'|^2 dA$$

where G is the electrode gap and Γ is the overlap integral between the applied electric field distribution (E) and the normalized optical field distribution (E'). The overlap integral is defined based on the total effective index change induced by the applied electric field directly at the aperture ($E_0 = V/G$). Therefore, if we calculated the overlap integral, the index change can be simply obtained from the above equation (3.22).

The overlap integral has been calculated for Ti-diffused LiNbO$_3$ waveguides with coplanar strip electrode[4] in which the optical mode is assumed to be Gaussian in width and Hermite Gaussian in depth. Since the overlap integral is not much dependent on the exact mode shape, the optical mode of this GaAs ridge waveguide is transformed to the Gaussian distribution based on the equivalent mode power ($|E|^2$) and then, obtained the equivalent overlap integral from that of Gaussian distribution. For the GaAs ridge waveguide, the optical mode behaves sinusoidally in the ridge region and

exponentially decays outside the ridge which is very similar to the Gaussian or Hermite Gaussian distribution. Therefore, the horizontal and vertical full width (w_h and w_v) of the ridge mode are obtained at the $1/e$ mode intensities of the single mode distribution. The calculated horizontal and vertical full mode sizes are 4.6 and 2.1 µm, respectively, at 1.3-µm wavelength. The mode is about two-times wider in horizontal direction than in vertical direction because the effective index difference ($\doteq 0.0022$) between the ridge and the side slab waveguides is very small compared to that ($=0.02$) between the ridge and the substrate. For 4 µm electrode gap and 4.6 µm horizontal mode width, the overlap integral Γ ($=0.5$) of the coplanar strip section B has been obtained from the overlap integral for Gaussian mode distribution. In section A with the cross-tie overlay, the field overlap is very small since the horizontal electric field in the GaAs ridge is small due to the electric wall of the cross-tie overlay. Therefore, we neglected the field overlap of section A in the optimization of the figure-of-merit discussed in the next section. The mode sizes are also suitable for good mode-coupling to single mode fibers of which mode sizes are about 4-7 µm.

3.4.5. Optimum design

Optimum design of the structure has been carried out by maximizing the figure-of-merit (F.O.M.), which is defined by the 3-dB optical bandwidth (f_{3dB}) divided by the half-wave modulation voltage (V_π) as follows.

$$\text{F.O.M.} = \frac{f_{3dB}}{V_\pi}$$

The 3-dB optical bandwidth is defined based on the half degradation of modulated optical power in the linear modulation region. The 3-dB optical bandwidth corresponds

to the 6-dB electrical bandwidth since the modulated optical power is linearly proportional to the applied voltage in the linear region. In the design of conventional optical modulators, there is a trade-off between the bandwidth and the DC modulation voltage due to the phase velocity mismatch which limits the F.O.M.. In the proposed phase-velocity-matched modulator, minimization of the conductor loss, however, is more important because the bandwidth is mainly limited by frequency-dependent conductor loss, not by phase velocity mismatch.

Although the modulation of the electrode width helps to reduce the conductor loss, the excess modulation will make high discontinuity effect at the periodic junctions and very thick silicon nitride layer which is not suitable for device fabrication. Therefore, the thickness of the silicon nitride layer should be within 1 μm. The modulation voltage is proportional to the electrode gap (G) while the conductor loss decreases by the electrode gap and width at a given characteristic impedance. The effective field overlap, between the applied horizontal electric field and the optical mode, increases by the length ratio (l_B/l_A) between the two sections because the field overlap in section A is very small due to the cross-tie overlay. Therefore, in the case of the matched termination of the electrode, the refractive index change $\Delta n(f,V)$ induced by the applied voltage (V) and accumulated along the propagation direction[28] can be expressed by

$$\Delta n(f,V) = \frac{n^3 r_{41} V L}{2 G} \; F\left[\gamma, \Gamma, L, l_A/l_B\right] \qquad (3.23)$$

$$F \equiv \frac{\Gamma_B}{1 + l_A/l_B} \; \frac{1 - e^{\gamma L}}{\gamma L \, e^{\gamma L}} \qquad (3.24)$$

$$\gamma = \alpha + j\Delta \quad , \quad \Delta = \frac{2\pi f\left(n_e^m - n_e^l\right)}{c}$$

where α, Δ, Γ_B, G, L, and f are the attenuation constant of the modulation wave, the phase constant due to the effective index difference between the modulation and light waves ($n_e^m - n_e^l$), the overlap integral in section B, the electrode gap, the total modulator length, and the modulation frequency, respectively. $F(\gamma, \Gamma, L, l_A/l_B)$ is defined as a frequency-dependent modulation reduction factor due to attenuation, phase velocity mismatch, and field misoverlap. Therefore, the modulation bandwidth can be obtained from the frequency characteristic of this reduction factor F.

The half-wave modulation voltage is usually defined as a DC voltage required to make a half-wave phase change of an optical wave with open termination of the electrode. However, in this structure, two orthogonal waves, which have respectively $\pm45°$ polarizations from the vertical direction, experience opposite phase modulations. Therefore, the half-wave modulation voltage (V_π) of this structure can be calculated from the equation (3.23) by equating the cumulative phase shift to the quarter wavelength ($\lambda/4$) of the optical wave.

$$V_\pi = \frac{\lambda\, G\left(1 + l_A/l_B\right)}{2\, n^3 r_{41} L \Gamma_B} \tag{3.25}$$

3.5. Calculated bandwidth and modulation voltage

Optimum geometries of the cross-tie electrode and the GaAs ridge waveguide shown in Fig.3.1 are obtained by optimizing the figure-of-merit. For the optimized structure, in Fig.3.7 and Fig.3.8 are shown the effective indices, the attenuation
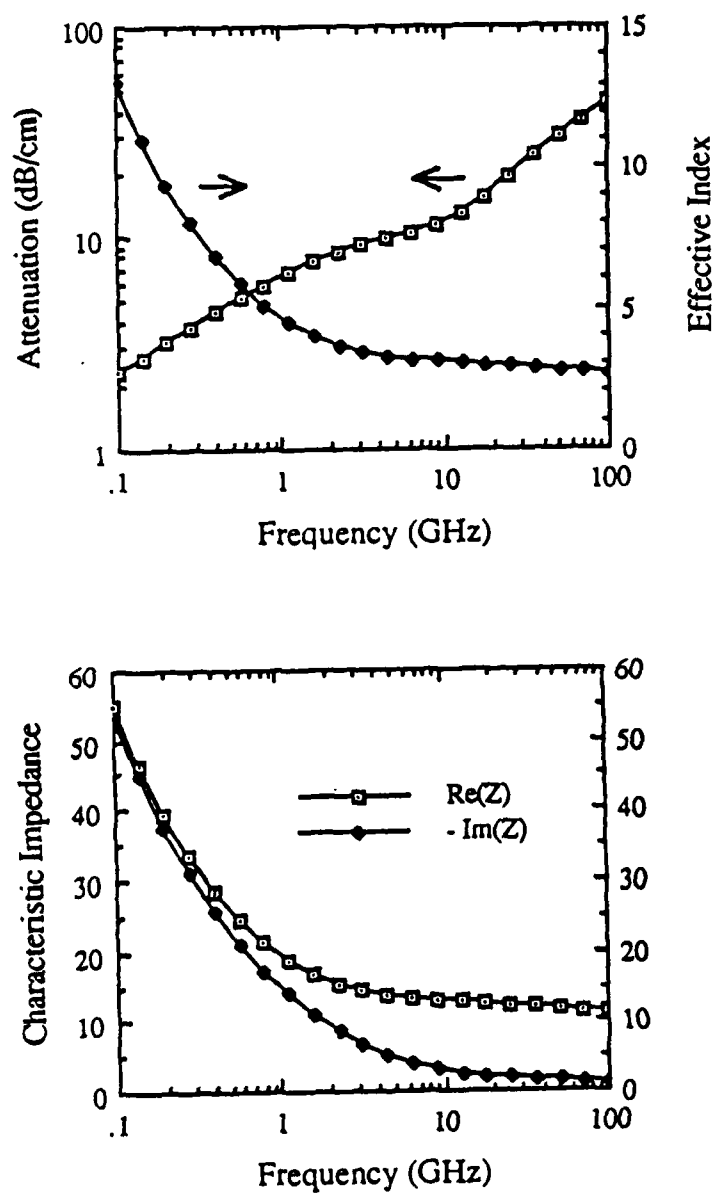
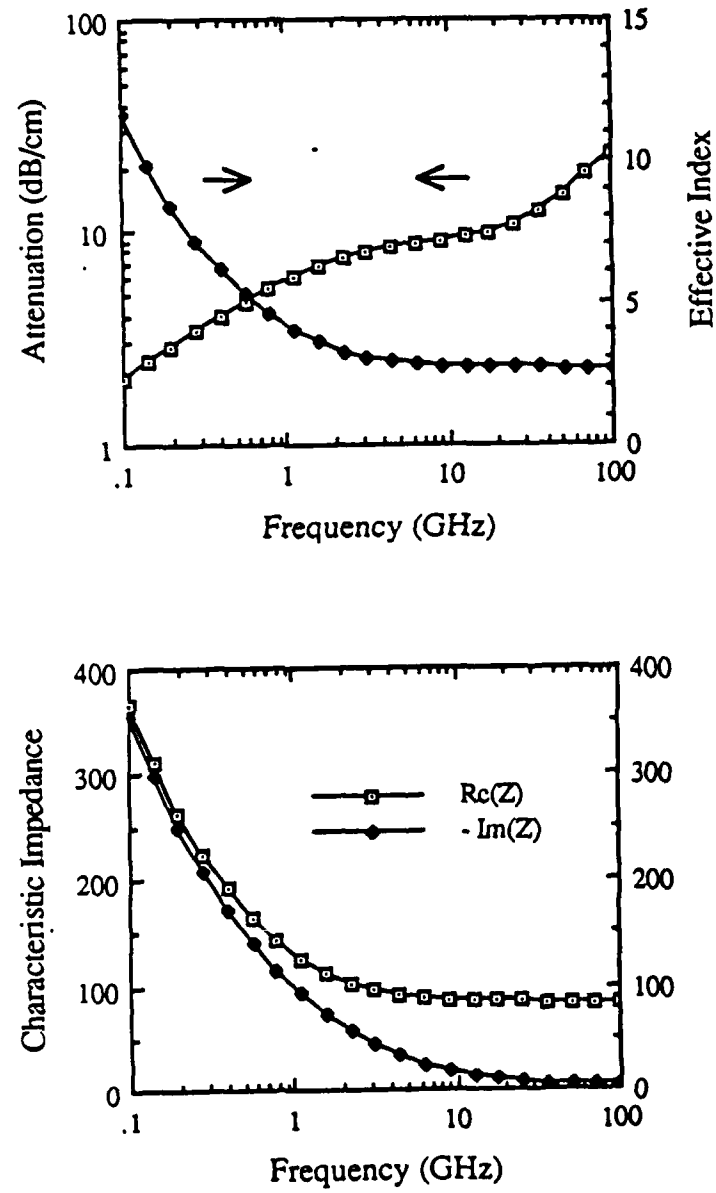**Fig. 3. 7.** Transmission characteristics of section A

47

Fig. 3. 8. Transmission characteristics of section B

constants and the characteristic impedances of the two sections, respectively. Section A has higher conductor loss and much lower characteristic impedance than section B while the effective indices are nearly the same. Those effective indices and characteristic impedances are very high and show high slow-wave effect at lower frequency region. That is because their distributed resistances are saturated at lower frequency region due to the high field penetration into the electrodes while the reactances of their shunt capacitances (C_0) become negligible at the lower frequency as shown in the equation (3.15). It is important to note that the saturation of the distributed resistance due to the field penetration dominates the slow-wave effect of lossy transmission lines at low frequencies.

The overall effective index as well as the attenuation constant of the slow-wave electrode are plotted in Fig.3.9. The effective index (3.4) of the optical waveguide at 1.3 µm is also shown as a horizontal dotted line in Fig.3.9. While the conductor loss is high in the upper frequency region, successfully satisfied is the simultaneous matching of the phase velocity and the characteristic impedance. The phase velocity mismatch in lower frequency region does not limit the bandwidth but just sightly degrades the modulation at lower frequencies. Therefore, the slow-wave structure is limited not by the phase velocity mismatch but by the attenuation. Note that, since the characteristic impedance is very high at low frequencies, especially at DC, the series connection of a capacitor to the termination resistor is needed in practice to improve the low-frequency characteristics.

In order to see the wideband characteristic clearly, the modulation reduction factor is shown in Fig.3.10 for the case of a 4-mm-long slow-wave electrode and 1.3 µm optical wavelength. Also shown is the optimum reduction factor of a conventional
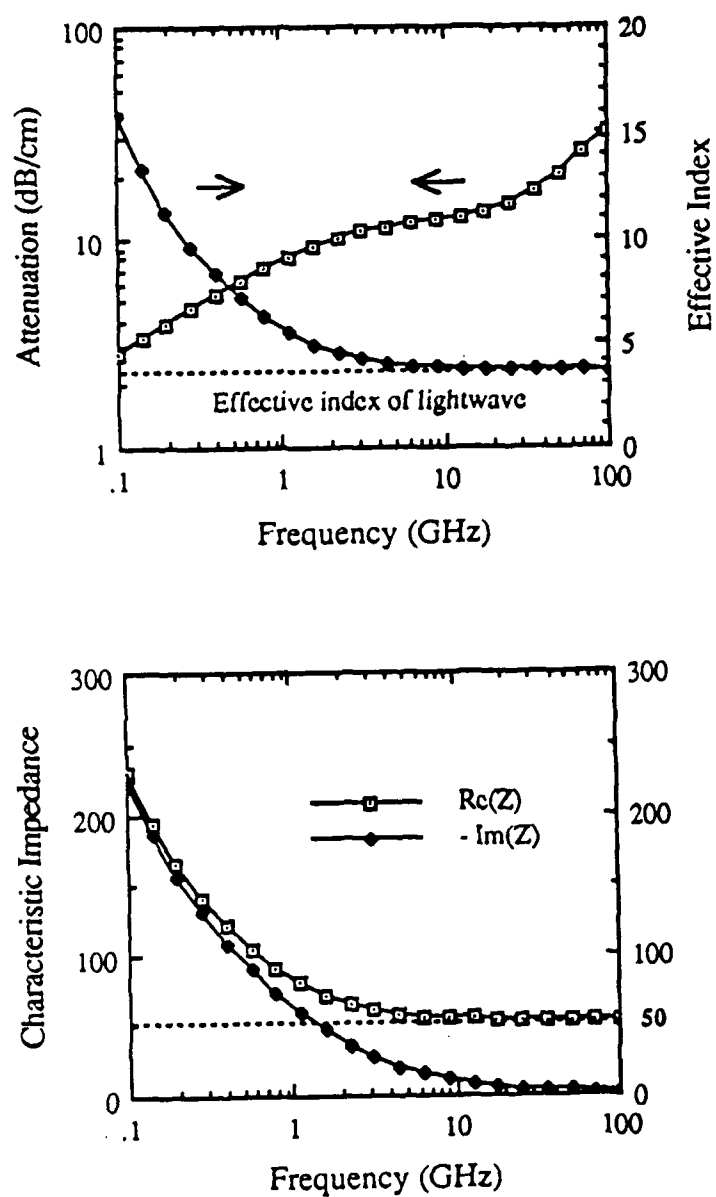
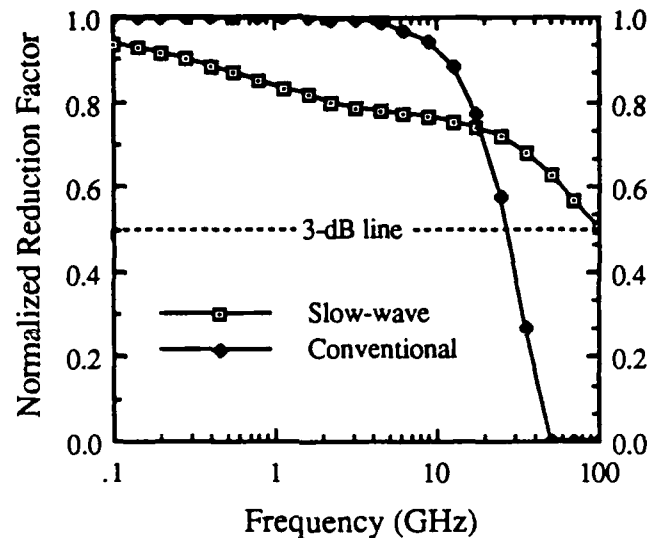Fig. 3. 9. Transmission characteristics of the slow-wave electrode

Fig. 3. 10. Modulation reduction factors of the slow-wave structure and conventional coplanar structure

structure[9] of the same electrode length and optical wavelength in which the modulation loss is neglected and only the phase velocity mismatch limits the frequency characteristics. The conventional structure has the 3-dB bandwidth of 30 GHz and the modulation reduction factor steeply degrades beyond the 3-dB bandwidth because of its sinc function behavior due to the phase-velocity mismatch. The slow-wave structure, however, has much wider 3-dB bandwidth (100 GHz) and the modulation reduction factor varies slowly over the 3-dB frequency. This slowly varying characteristic is preferable and more significant at higher frequencies and for longer modulators.

The calculated V_π (23 V) of the slow-wave structure is a little larger than that of the conventional electrode structure (20 V) due to the lower field overlap in section A. The figure-of-merit of 4 GHz/V is, however, much higher than that (1.5 GHz/V) of the conventional structure because of the perfect velocity match in the upper frequency region.

3.6. Fabrication and measurement

The 4 mm-long slow-wave structure has been build on a (100) face LEC-grown semi-insulating GaAs substrate which has a 500 μm thickness and a resistivity > 10^7 Ωcm. The waveguide ridge has been formed using the mesa etching technique on the pure GaAs substrate. The pure GaAs substrate is used to characterize the slow-wave electrode only since background carrier concentrations and imperfections of the epitaxial layers can be avoided in the pure substrate. The GaAs ridge however, cannot guide optical waves because the epitaxial layers for the vertical mode confinement have not been formed on the substrate. In the optimum design of the slow-wave electrode shown in Fig.3.1, the thickness of the silicon nitride layer (d) was 1μm. However, in this device fabrication, the thickness is limited to below 0.5 μm due to the large difference of the thermal expansion coefficients between GaAs and silicon nitride which makes cracks in the silicon nitride layer due to the temperature change during the device processing.

The device pictures shown in Fig.3.11 are taken in the vertical direction under a microscope. A narrow and long GaAs ridge can be seen between two large feeding pads tapered to reduce the reflection of the modulation wave. Periodic grids and a large
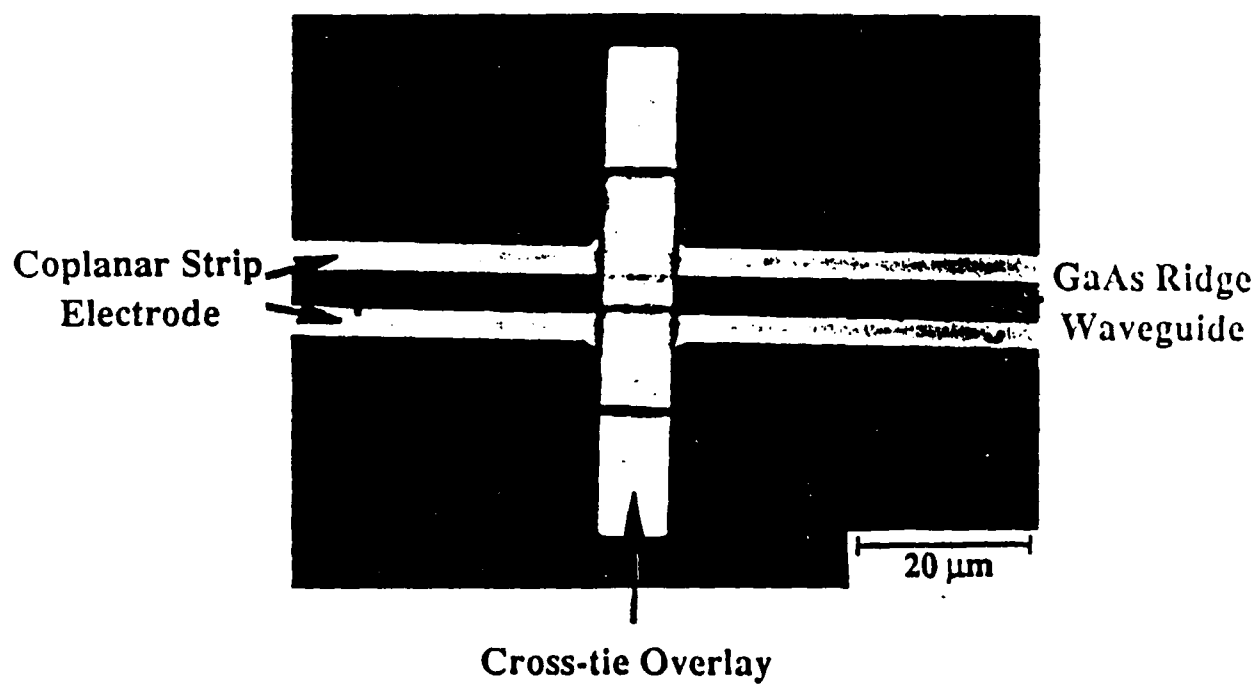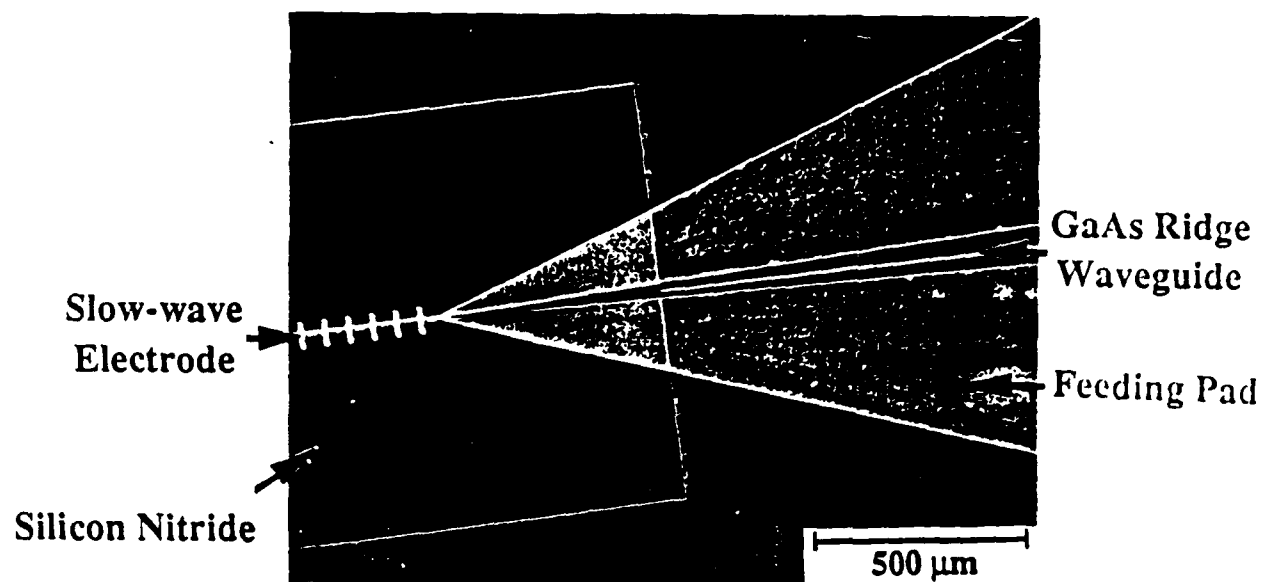
Fig. 3. 11. Photographes of the GaAs slow-wave optical modulator

rectangular area shown in the left side of Fig.3.11(a), are the slow-wave electrode and the silicon nitride area, respectively. Fig.3.11(b) shows one period of the slow-wave electrode. The GaAs ridge waveguide exists between two modulated coplanar strip electrodes, and a cross-tie overlay spaced by the silicon nitride layer is just on top of the wider strip section.

The actual thicknesses of the gold electrode and the silicon nitride measured using Dektek are 0.9 μm and 0.48 μm, respectively and the measured ridge height is 0.75 μm. The strip width (W=3.7 μm) and gap (S=4.3 μm) are measured using the microscope. The conductivity of the gold electrode (σ=35 S/μm) is obtained from the total DC resistance (R=64 Ω) of the electrode. The resistance measured between two feeding pads is almost infinite showing very high resistivity and negligible dielectric loss of the pure GaAs substrate.

The RF characteristics have been measured using HP 8510 network analyzer by terminating one end of the slow-wave electrode by short. The reflection (S_{11}) at the other end is measured using a tiny coplanar waveguide probe. Fig.3.12 shows the impulse response in time domain. High ref ction comes from the probe point corresponding to marker-1 in Fig.3.12 due to the mode mismatch between the coplanar waveguide probe and the coplanar strip electrode. The slow-wave electrode is between marker-2 and marker-3, and marker-3 corresponds to the short termination. Using the measured dimensional parameters, the transmission characteristics of the slow-wave electrode have been calculated and compared with the measured data in Fig.3.13. The equivalent shunt capacitance (C=0.037 pF) associated with the mode mismatch at the probe point has been obtained by matching the calculated data with the measured data.

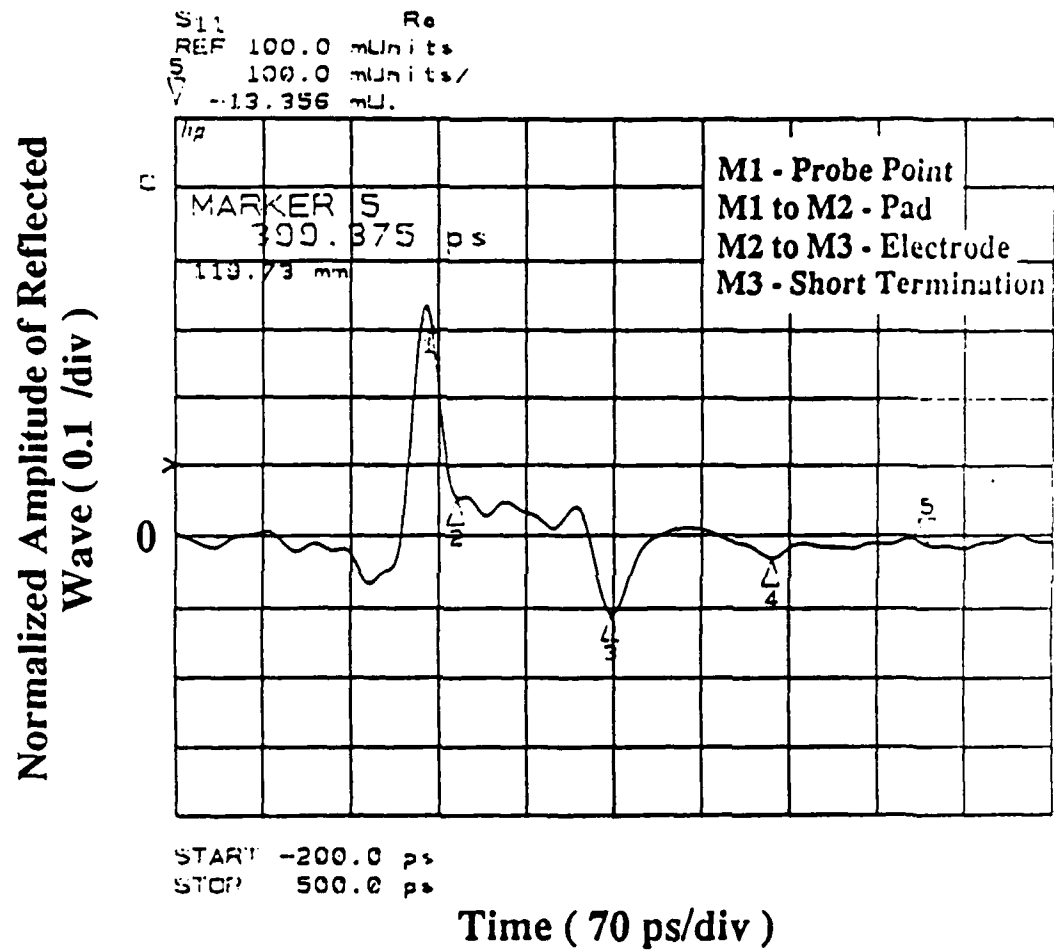**Fig. 3. 12.** Time-domain impulse response of the slow-wave electrode with a short termination
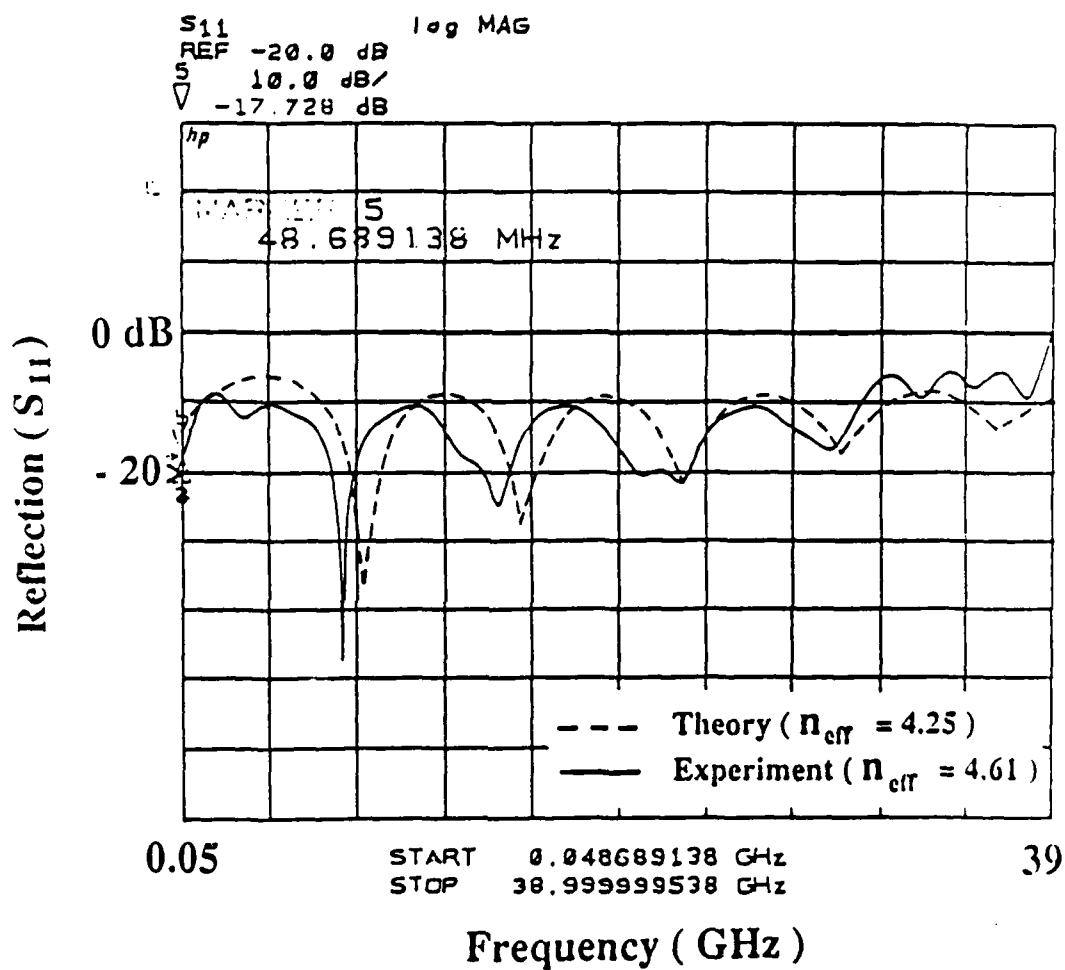
Fig. 3. 13. Frequency response (S₁₁) of the slow-wave electrode with short termination

The measured effective index (n_{eff}^m=4.61) obtained from the frequency interval of the resonant frequencies is much larger than that (n_{eff}^m=2.65) of conventional coplanar electrodes and agrees very well with the calculated one (n_{eff}^m=4.25). The slight deficiency mainly comes from the discontinuity capacitance between the cross-tie section and the normal coplanar strip section which enhances the slow-wave effect.

3.7. Conclusion

A GaAs traveling-wave optical modulator using a modulated coplanar strip electrode with periodic cross-tie overlays has been described in this chapter. Because phase velocity matching is satisfied using the slow-wave electrode, the figure-of-merit of this structure is mainly limited by the relatively high conductor loss. Therefore, in order to reduce the conductor loss, the electrode width is periodically modulated. The dominant conductor loss has been calculated in the wide ranges of frequency and field penetration using the phenomenological loss equivalence method. Optimization of the structure has been carried out by maximizing the figure-of-merit defined by the modulation bandwidth divided by the modulation voltage. For the optimized 4mm-long device at 1.3μm light wavelength, the 3-dB bandwidth of 100 GHz has been obtained which is much wider than the bandwidth limit (30 GHz) of conventional structures limited by the phase velocity mismatch. Although the calculated modulation voltage of 23 V is a little higher than that (20 V) of a conventional structure due to the slightly lower field overlap in section A, the overall figure-of-merit (4 GHz/V) is much larger than that (1.5 GHz/V) of the conventional structure. The slow-wave structure has been build on a semi-insulating GaAs substrate with the reduced thickness (0.48 μm) of the silicon nitride layer due to the fabrication difficulty of the thick silicon nitride layer.

The measured effective index (n_{eff}^m=4.61) is much larger than that (n_{eff}^m=2.65) of conventional coplanar electrodes and agrees very well with the calculated one (n_{eff}^m=4.25). The slight deficiency mainly comes from the discontinuity capacitance between the cross-tie section and the normal coplanar strip section which enhances the slow-wave effect.

Chapter 4

Wideband and Low Return Loss Coplanar Strip Feed
using an Intermediate Microstrip Line

4.1. Introduction

A very wideband and low return loss feed for coplanar strip line (CPS) is required for broadband electro-optic devices which use the CPS as the electrodes such as the optical modulator using coplanar strip slow-wave electrode shown in the previous chapter and the other CPS devices[9]. However, no theoretical as well as experimental work has yet been published on the CPS feed because the CPS has not been used frequently. Slotline feeds using coaxial and open microstrip lines[29] are not directly applicable to the wideband CPS feed due to their frequency-dependent transformation ratios and the bandpass characteristics of the open microstrip. The direct connection of the coaxial line to the CPS is not practical for the monolithic integration with the devices as well.

This chapter shows a new and practical CPS feed using a microstrip between coaxial and CPS lines which can be monolithically integrated with the devices[30]. The intermediate microstrip line is used to minimize the discontinuity effect as well as the frequency-dependent transformation ratio between the coaxial and CPS lines and then, to make a wideband and low return loss possible. A 15mm-long CPS electrode fed and terminated by two 11mm-long intermediate microstrip lines has been build and

measured using HP 8510 network analyzer. The measured and calculated return losses are below 13dB up to 18GHz and coincide with each other over a very wide bandwidth. An extended calculation using TDR data shows the return loss below 10dB up to 30GHz. If we make the structure monolithically small, the bandwidth can be increased much more and this coplanar strip feed will be more practical for the feeding of wideband electro-optic devices using the coplanar strip as the electrodes.

## 4.2. Configuration of the coplanar strip feed

Fig.4.1 shows the schematic of the CPS feed. Both open ends of a CPS line are perpendicularly connected to coaxial connectors through two intermediate microstrip lines. The intermediate microstrip lines are placed just on top of the CPS line. The ground planes of the microstrip lines are tapered and electrically connected to one strip of the CPS line with conducting epoxy; the microstrip conductors are welded to an internal edge of the other strip using gold ribbons. The dielectric substrate for the microstrip lines is very thin (127μm) and has a low dielectric constant (2.0). The dielectric substrate for the CPS line is very thick (3000μm) and has a dielectric constant of 10.0. Both the microstrip and CPS lines are designed for 50Ω characteristic impedance using quasi-static analysis. The gap and width of the CPS line are 58μm and 490μm, respectively, and the microstrip width is 385μm. The gold ribbons are 350μm wide and 250μm long.

4.3. Equivalent circuit

The equivalent circuit of this structure shown in Fig.4.2 can be obtained through a modification of the simplified model of coax-slot transition[31]. For the slot
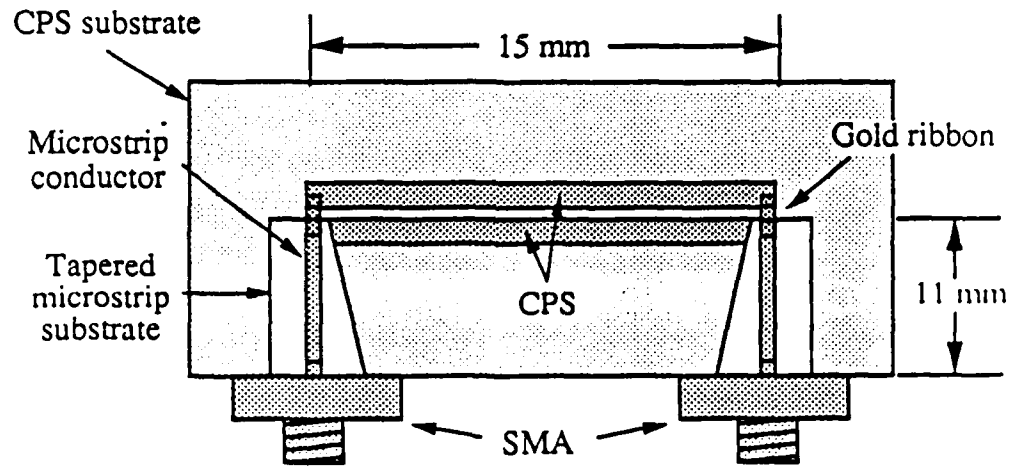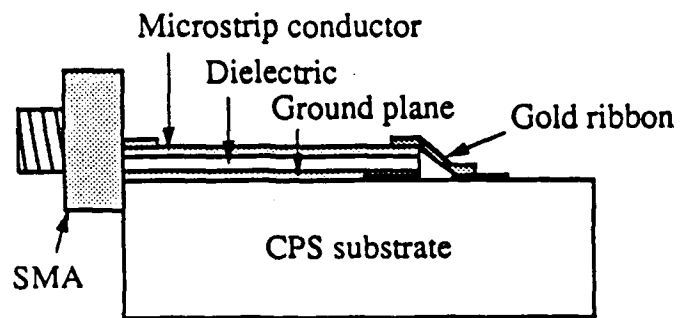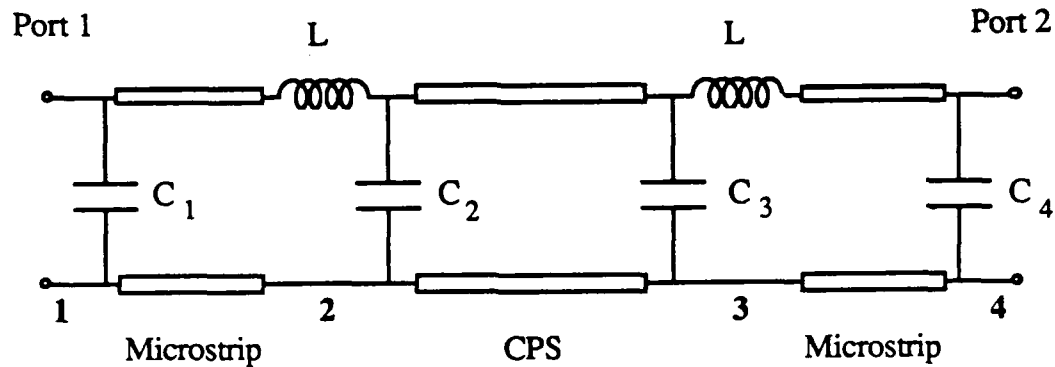
Fig. 4. 1. Schematic diagram of the coplanar strip feed:

(a) Top view and (b) Cross-section

Port 1   L   L   Port 2

1   2   3   4

Microstrip   CPS   Microstrip

1 and **4** : Microstrip to coax transitions

2 and **3** : Microstrip to CPS transitions

Fig. 4. 2. Equivalent circuit of the coplanar strip feed

line with very narrow aperture, the aperture field can be approximated by a line source of magnetic current at the aperture. Therefore, the longitudinal component of magnetic field (H_z) can be expressed by the Hankel function of first kind on the air side of the slot as follows[32].

$$H_z = A H_0^{(1)}(k_c r)$$ (4.1)

$$k_c = \frac{j 2\pi}{\lambda'} \sqrt{1 - \left(\frac{\lambda'}{\lambda}\right)^2}$$

where r and λ' are the distance from the aperture and the slot-mode wavelength, respectively. Using the identity of the Hankel function

$$\frac{d\left[H_0^{(1)}(x)\right]}{d x} = -H_1^{(1)}(x)$$ (4.2)

the circular component of electric field (E_ϕ) can be expressed by

$$E_\phi = \frac{j\omega\mu}{k_c^2}\frac{\partial H_z}{\partial r} \approx \frac{-\eta\frac{\lambda'}{\lambda} A\, H_1^{(1)}(k_c r)}{\sqrt{1-\left(\frac{\lambda'}{\lambda}\right)^2}} \tag{4.3}$$

If we define the transformation ratio (n) as the voltage V(r) along a semicircular path at a radius r divided by the voltage directly across the slot, the ratio can be obtained from the electric field (E_ϕ) as

$$n = \frac{V(r)}{V_0} = \frac{\pi}{2}k_c r\left| H_1^{(1)}(k_c r)\right| \tag{4.4}$$

For the geometry of the microstrip-coplanar strip transition shown in Fig.4.1, the calculated transformation ratio is approximately unity over a very wide band. That is because the gold ribbon is very close to the CPS gap and the equivalent semiloop has a very small radius. Therefore, the transformation at the microstrip-CPS transition can be simplified by a small series inductance (L=37pH) of the gold ribbon calculated by flat wire model.

Although open ends of the microstrip and the CPS can be accounted for by fringe capacitances in the equivalent circuit, they cannot be precisely calculated at the microstrip-CPS transition because of the gold ribbon. Therefore, lumped equivalent capacitances (C_2=0.059 and C_3=0.050pF) at the two transitions are calculated from time-domain reflectometry (TDR) measurement using HP 8510B automatic network analyzer and these values are used in all further calculations. The coax-microstrip transitions are simplified by the dominant shunt capacitance (C_1 and C_4=0.0049pF) of an open microstrip[33] because the fringe capacitance of the open coax and the series

inductance at the transition are negligible in coax-microstrip model[34]. Conductor losses of the microstrip and the CPS, calculated using incremental inductance method[35], are 0.015 and 0.17 dB/cmGHz$^{1/2}$, respectively.

4.4 Measurement of the return loss and discussion

Experimental measurement of this structure has been done using HP 8510B network analyzer. Reference planes are set at the two coax-microstrip transitions. After calibration, TDR data for a step input and S-parameters are measured. From TDR data shown in Fig.4.3, all parameters in the equivalent circuit are calculated and compared with the theoretical values. Except for the fringe capacitances at the microstrip-CPS transitions, they are in reasonable agreement with the theoretical values. In Fig.4.3, it can be seen that most of reflection comes from capacitive discontinuities at the microstrip-CPS transitions corresponding to the marker points 2 and 3. The coax-microstrip discontinuities, corresponding to marker points 1 and 4, have small reflections and they are mostly resistive because the coax and the microstrip have slightly different actual characteristic impedances. Measured actual characteristic impedance(48.5) of the CPS line is also sightly lower than 50(Ω). Small inductances of the gold ribbons contribute little to the reflections and most of the conductor loss exists in the CPS line.

In Fig.4.4, the measured return loss is compared with the theoretical one calculated from the equivalent circuit. They exhibit close agreement over a very wide bandwidth and show the return loss below 13dB up to 18GHz. Although the measured data are within 18GHz bandwidth of the measurement set-up, the extended calculation using the equivalent circuit and the parameters calculated from the TDR measurement in
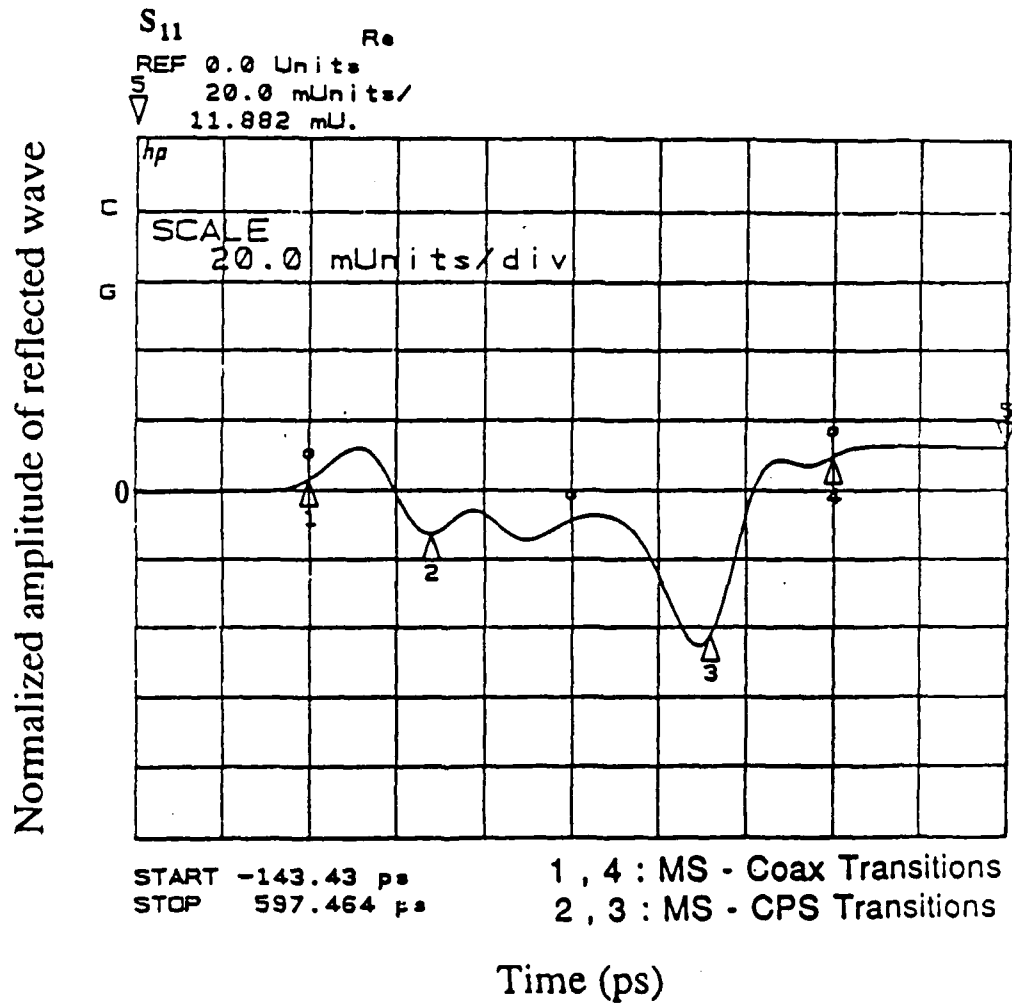
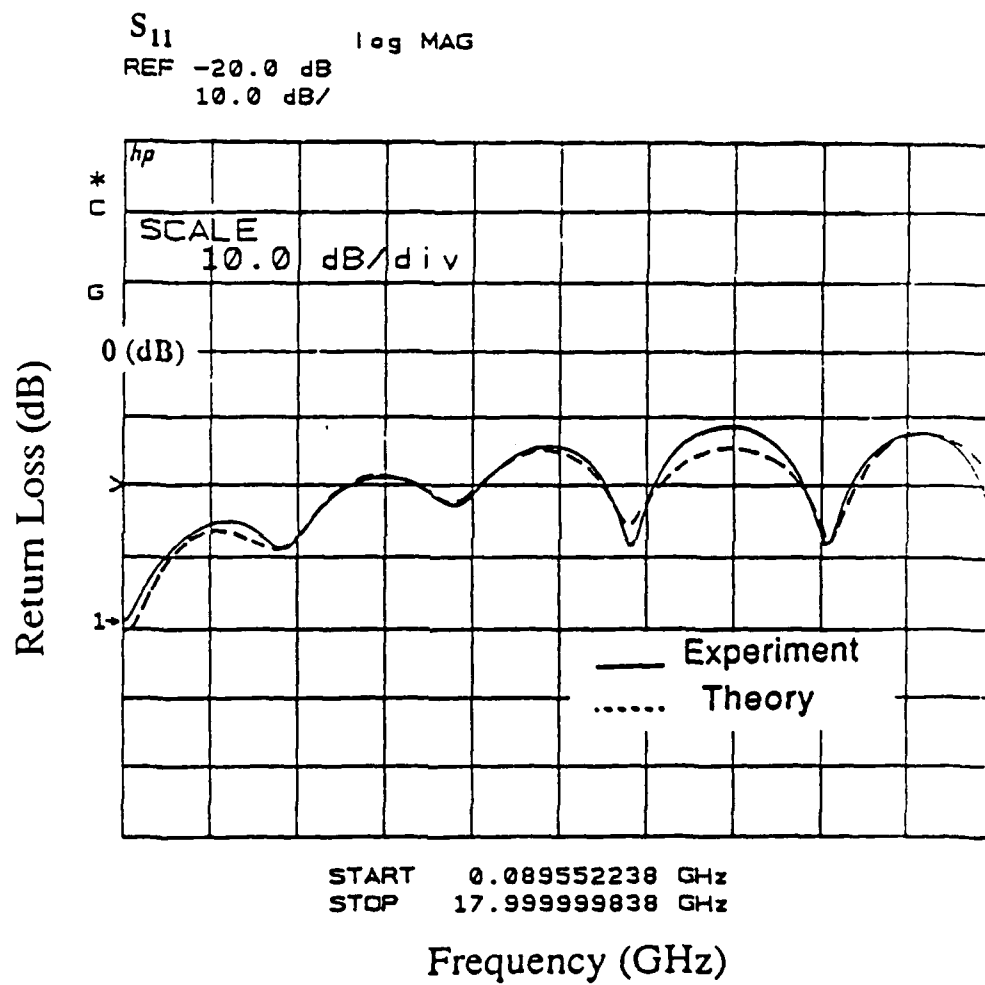Fig. 4. 3. Time-domain reflectometry response for a step input
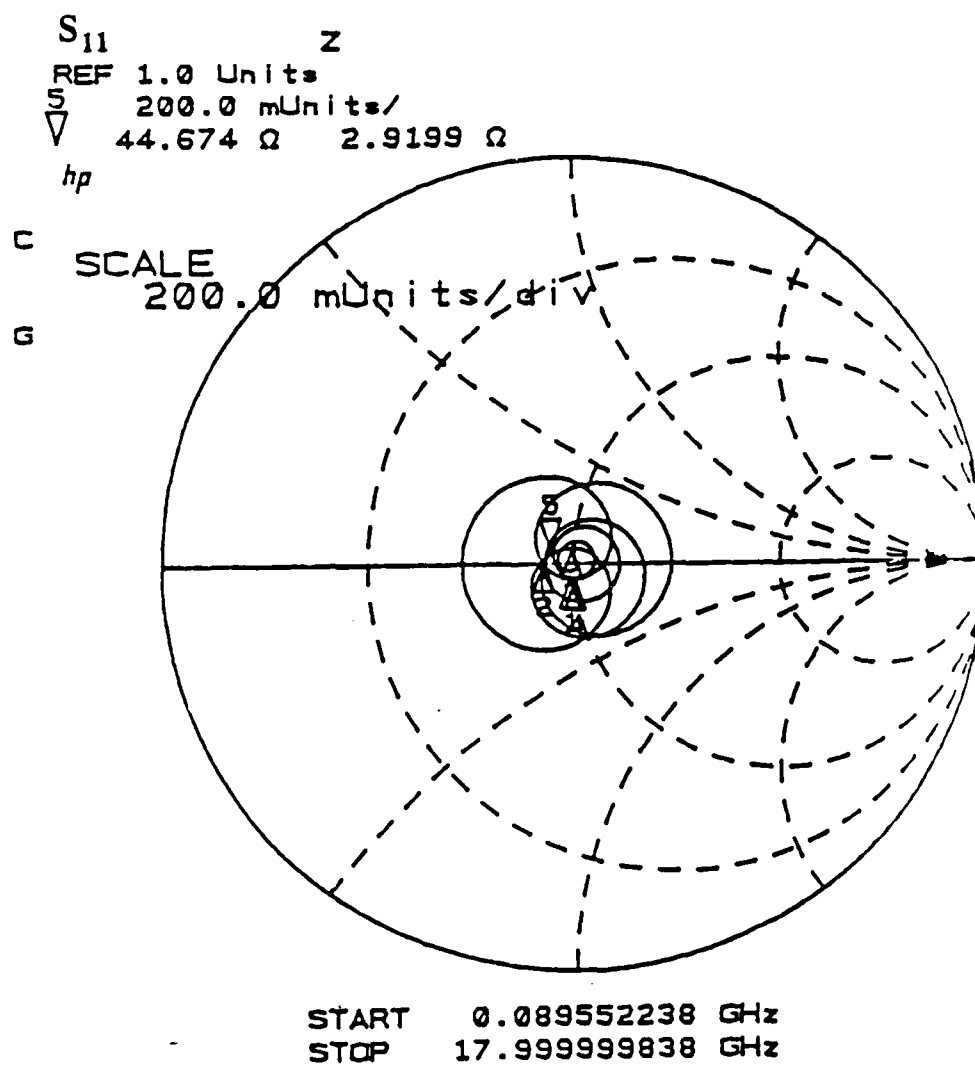
Fig. 4. 4. Return loss (S_{11})

Fig. 4. 5. Polar plot of S 11

the bandwidth shows the return loss below 10dB up to 30 GHz. We can also see the small reflection clearly in Fig.4.5. showing the S_{11} in polar coordinate. Throughout the measurement of transmission characteristics(S_{21}), it is observed that radiation and substrate modes take place at the microstrip-CPS transitions and these modes create some resonance and additional loss to the transmission characteristics. However, these modes have minor effect on the reflection and they are neglected in the theoretical calculations.

In order to minimize the return loss and to increase the bandwidth, close proximity of the gold ribbons to the CPS gap and small capacitances in the discontinuities are necessary. These can be accomplished simultaneously using very thin microstrip substrate. However, since the thinner the substrate is, the narrower the microstrip for the 50(Ω) characteristic impedance, very thin substrate as well as narrow microstrip result in large discontinuity capacitance at the microstrip-coax transition. Therefore, the substrate thickness should be chosen carefully and a tiny coaxial connector is also helpful for practical usage. Tapering of the microstrip ground plane affects the reflection less than the microstrip-CPS transitions. However, it is needed to minimize the transition area because the ground plane reduces the characteristic impedance of the CPS line near the transition.

4.5. Conclusion

A new and practical CPS feed of wideband and low return loss has been achieved using an intermediate microstrip line between coax and CPS lines. The measured and calculated return losses are in good agreement and below 13 dB up to 18GHz. The extended calculation of the return loss based on the equivalent circuit and

the parameters calculated from TDR measurement, shows the return loss below 10dB up to 30GHz. This wideband CPS feeding can be directly applied to the wideband feeding of electro-optic devices that use the CPS line as their electrodes such as the traveling-wave optical modulator shown in the previous chapter. This structure can be integrated monolithically with the optical devices on a GaAs substrate.

Chapter 5

GaAs Traveling-wave Optical Modulator using a Modulated Coplanar Waveguide Electrode with Periodic Cross-tie Overlays

5.1. Introduction

In an effort to reduce the transit time difference of GaAs traveling-wave optical modulators, the principles of a slow-wave structure using periodic cross-tie overlays has been previously described and applied to a GaAs traveling-wave optical modulator using a modulated coplanar strip electrode with the cross-tie overlays. In the new structure, the phase velocity matching as well as the impedance matching to $50(\Omega)$ have been successfully satisfied over a very wide frequency range by reducing the phase velocity of the modulation wave using the slow-wave electrode. For the practical use of the device, also described is a proposed very wideband feeding of the coplanar strip electrode using an intermediate microstrip line between the coplanar strip and a coax.

This chapter describes a GaAs traveling-wave optical modulator using a modulated coplanar waveguide with the cross-tie overlays and presents the design method including design considerations for the optimum structure[36],[37]. Since this optical modulator is based on the coplanar waveguide electrode, we can put two optical waveguides between a center conductor and two half ground planes. Therefore, this structure will be suitable for amplitude modulators such as interferometer or coupled-

69

waveguide modulator while the coplanar strip type is preferable for very high frequency phase modulation such as for optical heterodyne communication.

This coplanar waveguide structure has been analyzed using the spectral domain analysis[38], which is a fullwave analysis including dispersion characteristics, for each section and by the same application of the Floquet's theorem to the periodic array as in the coplanar strip case. The conductor loss has been calculated using the proposed phenomenological loss equivalence method[44]-[46]. The fullwave analysis shows the overall dispersion predominantly comes from the periodic array and the high conductor loss and hence, the quasi-static analysis for the coplanar strip structure is valid. This structure can also be designed to satisfy the phase velocity and impedance matching conditions simultaneously over a broad spectral bandwidth. Therefore, the modulation bandwidth is greatly increased for the case of zero conductor loss. However, since the coplanar waveguide structure has higher conductor loss than the coplanar strip structure, it has higher modulation voltage and lower bandwidth resulting in lower figure-of-merit.

5.2. Structure description

The slow-wave structure shown in Fig.5.1. consists of an infinite array of more capacitive section A with a cross-tie overlay and more inductive section B without the overlay on the coplanar waveguide. The center strip of the coplanar waveguide is also periodically modulated to reduce the conductor loss: sections A and B have wider and narrower strips, respectively. The period chosen is much smaller than the propagation wavelength for a uniform transmission line. The proposed slow-wave optical modulator can be fabricated as follows as shown in Fig.5.1. Firstly, an AlGaAs layer

Section A   Section B

Slow-wave electrode :
$W_A = 5$, $S_A = 8$, $l_A = 5$
$W_B = 2$, $S_B = 2$, $l_B = 40$
$d = 0.5$, $t = 0.7$, $h = 500$

GaAs waveguide :
Index difference(Δn) = 0.1
$a = 6.5$, $b = 3.0$
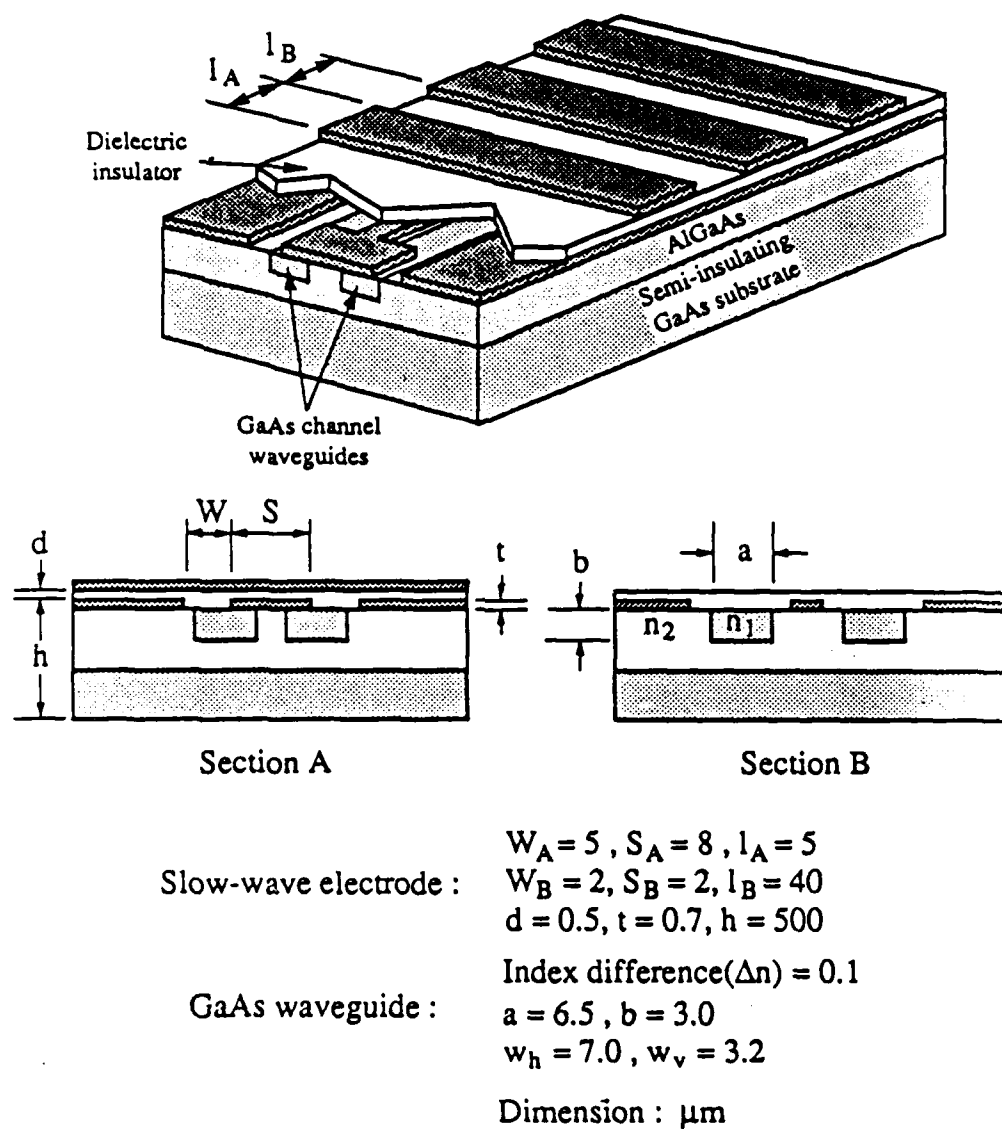$w_h = 7.0$, $w_v = 3.2$

Dimension : μm

Fig. 5. 1. Schematic configuration of GaAs traveling-wave optical
modulator using coplanar waveguide slow-wave electrode

is epitaxially grown on a semi-insulating GaAs substrate. Two GaAs optical channel waveguides are then embedded in the AlGaAs epitaxial layer by epitaxial growing and mesa etching technique[39]. Next, coplanar waveguide electrodes are fabricated on the top surface of the AlGaAs layer and an insulating dielectric layer is deposited on the electrode. Finally, periodic metal cross-tie overlays are fabricated on the dielectric layer.

The dielectric loss of the modulation wave and the optical loss due to free carrier absorption can be neglected in this semi-insulating GaAs layers if the background concentrations of the epitaxial layers are less than $10^{14}/cm^3$ [19]. The embedded GaAs channel waveguides are used to minimize the cross-talk between the optical waveguides because the horizontal mode size can be reduced using large index difference between GaAs core and AlGaAs clad layers. The crystal orientation is the same as the coplanar strip case shown in chapter 3 to use the highest electro-optic effect. Since the modulation electric fields (E) in the two optical waveguides are in opposite directions each other, two light waves in the optical waveguides experience opposite phase shifts over the interaction length (L) due to the index change ($\delta n \sim n^3 r_{41} E/2$) induced by the electro-optic effect. In order to accumulate the local phase shifts along the waveguide completely, the phase velocity matching between the optical and modulation waves has been accomplished by the slow-wave structure using periodic cross-tie overlays.

5.3. Spectral domain analysis of the slow-wave electrode

The numerical analysis of this structure has been carried out by a full-wave analysis using the standard spectral domain method[38] for each section and by an application of the Floquet's theorem to the periodic array. The dielectric constant is

assumed to be uniform in the substrate region up to millimeter wave frequency range because a small variation of the dielectric constant is enough to form a well-guiding optical waveguide. The thin conductor thickness is incorporated into the effective strip width and gap using the empirical formulas[20] to make the structure planar and simplify the spectral domain analysis. Therefore, the cross-tie section A is a coplanar waveguide with an electric wall spaced by a dielectric layer and section B is a thin coplanar waveguide with a thin dielectric cover layer on GaAs substrate. The spectral domain analysis is one of well-known standard full-wave analyses which is very powerful for planar structures because of the high computation efficiency and the easy formulation. Since the analysis method is well-known and straight forward, the simple formulation procedure as well as the basis function used in this structure will be described.
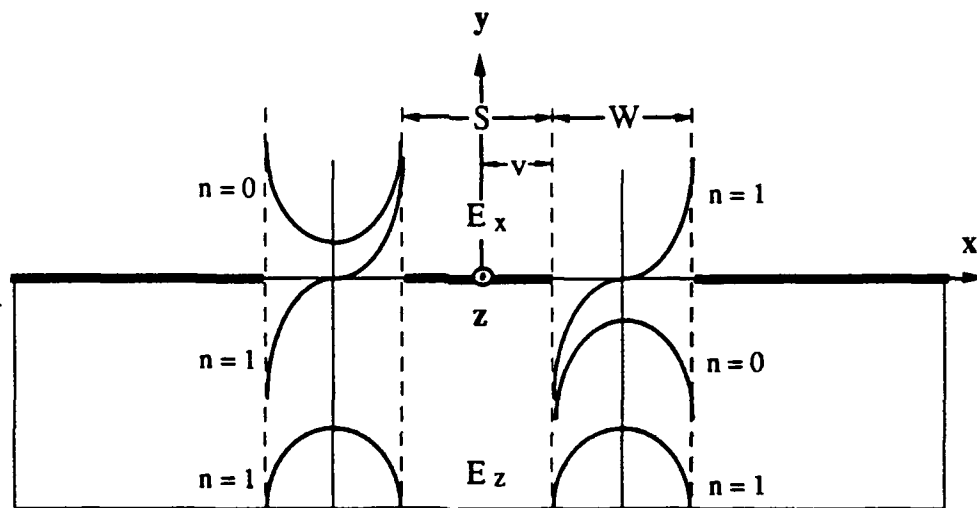

Fig. 5. 2. Coordinate and basis function used in the spectral domain analysis

Since this coplanar waveguide structure has the wide ground plane as shown in Fig.5.2., it is better to expand the unknown transverse and longitudinal electric fields (E_x and E_z) in the slot regions and apply the Galerkin's procedure to the electric fields in order to reduce the number of basis functions needed and increase the computation efficiency. The electric fields in the slot regions have been expanded by a set of basis functions and then, we dealt with the following algebraic equations in spectral domain associated with the coupled integral equations in space domain.

$$\widetilde{Y}_{xx}(\alpha,\beta)\ \widetilde{E}_x(\alpha) + \widetilde{Y}_{xz}(\alpha,\beta)\ \widetilde{E}_z(\alpha) = \widetilde{J}_x(\alpha)$$
$$\widetilde{Y}_{zx}(\alpha,\beta)\ \widetilde{E}_x(\alpha) + \widetilde{Y}_{zz}(\alpha,\beta)\ \widetilde{E}_z(\alpha) = \widetilde{J}_z(\alpha) \tag{5.1}$$

where $\widetilde{Y}$, $\widetilde{E}$, and $\widetilde{J}$ are the Green's admittance function, the slot electric fields, and the currents on the conductors for a spectral component (α,β) corresponding to (x,y) in space domain. Then, by applying the Galerkin's procedure in the spectral domain which expands the electric fields by basis functions and takes inner products of the resultant equations, the previous equations finally become homogeneous matrix equations by virtue of Parseval' theorem.

$$\sum_{n=0}^{M} K_{mn}^{xx} c_n + \sum_{n=1}^{N} K_{mn}^{xz} d_n = 0 \ , \quad m = 0, 1, ---, M$$
$$\sum_{n=0}^{M} K_{mn}^{zx} c_n + \sum_{n=1}^{N} K_{mn}^{zz} d_n = 0 \ , \quad m = 1, 2, ---, N \tag{5.2}$$

where $K_{mn}^{ab} \equiv \int_{-\infty}^{\infty} \widetilde{E}_{am}(\alpha)\ \widetilde{Y}_{ab}(\alpha,\beta)\ \widetilde{E}_{bn}(\alpha)\ d\alpha$ representing the inner product between the mth basis function of a-component electric field ($\widetilde{E}_{am}$) and the nth current function of b-component ($\widetilde{Y}_{ab}\widetilde{E}_{bn}$). c_n and d_n are the unknown coefficients of the nth basis

function for x and z-component of the aperture electric field. Therefore, the propagation constant (β) can be obtained by solving the nontrivial solution of the eigenvalue equation (5.2).

Any set of the basis functions can be chosen if the set is complete and preferably orthogonal in the slot regions. There are several additional criteria[40] for the convergence efficiency and accuracy since this spectral domain method has variational nature. The electric field near conductor edge should behave properly to ensure finite field energy and to achieve fast convergence (i.e. normal field $(E_x) \sim \rho^{-1/2}$ and tangential field $(E_z) \sim \rho^{1/2}$ at the distance ρ from the conductor edge). In addition, the basis functions should also be chosen to have close resemble to the actual field distribution by any physical insight available. Finally, the closed form expressions of the Fourier transform should be available to reduce the numerical computation. The following set of basis functions are employed because they satisfy all the previous criteria.

$$
E_{xn}(x) = \begin{cases}
\dfrac{\cos\left(n\pi\dfrac{x+v}{w}\right)}{\sqrt{1 - \left[\dfrac{2(x+v)}{w}\right]^2}} - \dfrac{\cos\left(n\pi\dfrac{x-v}{w}\right)}{\sqrt{1 - \left[\dfrac{2(x-v)}{w}\right]^2}} & n = 0, 2, 4, \cdots \\[6mm]
\dfrac{\sin\left(n\pi\dfrac{x+v}{w}\right)}{\sqrt{1 - \left[\dfrac{2(x+v)}{w}\right]^2}} + \dfrac{\sin\left(n\pi\dfrac{x-v}{w}\right)}{\sqrt{1 - \left[\dfrac{2(x-v)}{w}\right]^2}} & n = 1, 3, 5, \cdots
\end{cases}
$$

$$E_{zn}(x) = \begin{cases} \dfrac{\cos\left(n\pi\,\dfrac{x+v}{w}\right)}{\sqrt{1-\left[\dfrac{2(x+v)}{w}\right]^2}} + \dfrac{\cos\left(n\pi\,\dfrac{x-v}{w}\right)}{\sqrt{1-\left[\dfrac{2(x-v)}{w}\right]^2}} & n = 1, 3, 5, \cdots \\[4ex] \dfrac{\sin\left(n\pi\,\dfrac{x+v}{w}\right)}{\sqrt{1-\left[\dfrac{2(x+v)}{w}\right]^2}} - \dfrac{\sin\left(n\pi\,\dfrac{x-v}{w}\right)}{\sqrt{1-\left[\dfrac{2(x-v)}{w}\right]^2}} & n = 2, 4, 6, \cdots \end{cases} \tag{5.3}$$

where $v=(s+w)/2$ and the functions are defined only over the slots ; the first and the second terms are valid for $x>0$ and $x<0$, respectively.

Since this structure is not a pure TEM line, the definition of the characteristic impedance is not unique. The most reasonable definition is based on the time-averaged power (P) flowing the propagation direction (z) and the voltage (V) across the slot as follows[41].

$$Z_0 = \frac{V^2}{2P} \tag{5.4}$$

where $V = \int_{Slot} E_x(x)\,dx$ and $P = \text{Re}\left[\iint_- \left(\bar{E} \times \bar{H}^*\right).\,\hat{z}\,dx\,dy\right]$

The E and H fields can be calculated from the eigenvectors of the eigenvalue equation (5.2). In order to simplify the power calculation, we transform the equation in space domain (x) to that in the spectral domain (α) using the Parseval's theorem. Therefore, the following power equation can be readily integrated since we know the y-variation of the α-component from the planewave solution in y-direction.

$$P = \text{Re}\iint_- \left[\widetilde{E}_x(\alpha,y)\widetilde{H}_y^*(\alpha,y) - \widetilde{E}_y(\alpha,y)\widetilde{H}_x^*(\alpha,y)\right]d\alpha\,dy \tag{5.5}$$

5.4. Optimum design

The optimization of this structure can be done by maximizing the figure-of-merit in the same way as in the coplanar strip case. Since the coplanar waveguide has higher conductor loss than the coplanar strip at high characteristic impedance, this coplanar waveguide structure has higher conductor loss than the coplanar strip structure due to the high characteristic impedance of section B. The overlap integral can be approximately obtained in the same manner as in the coplanar strip case because the electric field distribution of the coplanar waveguide is similar to that of corresponding coplanar strip in the middle of the gap where the optical waveguides exist.

5.4.1. Design of the slow-wave electrode

This slow-wave structure has many design parameters for the coplanar waveguide, the dielectric layer, and the cross-tie overlays which allow wide design flexibility for the simultaneous matching of the phase velocity and the impedance. The two main design requirements are the phase velocity matching and the impedance matching given by

$$n_e^m = n_e^l \text{ and } Z_0 = 50 \, (\Omega) \qquad (5.6)$$

where n_e^m, n_e^l and Z_0 are the effective indices of the modulation and light waves and the characteristic impedance, respectively.

Additional design considerations[4] should be imposed for high modulation efficiency, low conductor loss, and realizable dimensions. High field intensity can be achieved by minimizing the realizable electrode gap while low current density for the

small conductor loss requires thick and wide electrodes. Since the applied electric fields in sections A and B are mostly concentrated in the dielectric and the substrate layers, respectively, it is necessary to increase the length ratio between the two sections (l_B/l_A) in order to achieve the high effective field overlap (Γ) between the applied field and the optical mode. The one period length ($l_A + l_B$) for a fixed length ratio (l_B/l_A)) is limited by the minimum achievable feature size of the electrode. Silicon nitride is chosen for a dielectric material because of its high dielectric constant and high field strength which allow high slow-wave effect and high power operation, respectively.

5.4.2. Design of the optical channel waveguide

The optical waveguide must be designed interactively with the electrode design to enhance the field efficiency of the modulation wave. The main factors for the optimum design are the effective index, the mode size and the relative alignment to the electrodes. Since the composition ratio (x) of the $Al_xGa_{1-x}As$ layer can be accurately controlled over a wide range using epitaxial growing techniques, the difference between the refractive indices of the GaAs channel (n_1) and the AlGaAs clad (n_2) ($\Delta n = n_1 - n_2 \approx 0.62 \Delta x$, where Δx is the composition ratio difference)[42] can be made large enough for the high field confinement of the optical mode. The mode penetration into the dielectric layer is also quite small due to the high refractive index difference between the dielectric and the GaAs layers. Therefore, the effective index (n^l_e) and the horizontal and the vertical mode sizes (w_h, w_v) can be approximately expressed as follow for a well-guided fundamental mode[43].

$$n_e^1 = \sqrt{n_1^2 - \left(\frac{\lambda}{2a}\right)^2 - \left(\frac{\lambda}{2b}\right)^2}$$

$$w_h = a + \frac{0.23\,\lambda}{\sqrt{\Delta n\ n_2}}$$

$$w_v = b + \frac{0.12\,\lambda}{\sqrt{\Delta n\ n_2}}$$

(5.7)

where a and b are the horizontal and the vertical dimensions of the rectangular waveguide and λ is the free space wavelength. Although small mode size is advantageous for high field overlap, the minimum mode size should be comparable to that of typical single mode fiber (≈ 7 μm) for low coupling loss. Therefore, in the optimum design there is a tradeoff between the high field overlap and the low coupling loss.

5.5. Calculated results and discussion

There are many possible combinations of multiple design parameters for the simultaneous matching of the phase velocity and impedance. An optimum design shown in Fig.5.1. is obtained by considering the design and fabrication feasibility as well as maximizing the figure-of-merit. In order to reduce the conductor loss and make the fabrication easy, the minimum strip width (S_B) of section B is fixed to 2μm and then, the gap ($W_B=8\mu$m) is obtained. The strip width of section A (S_A) is extended to 8μm in order to reduce the conductor loss. The conductor thickness (t=0.7μm) is chosen for easy fabrication and accurate analysis. The total modulator length and the light wavelength are 4mm and 1.3μm, respectively as in the coplanar strip case.
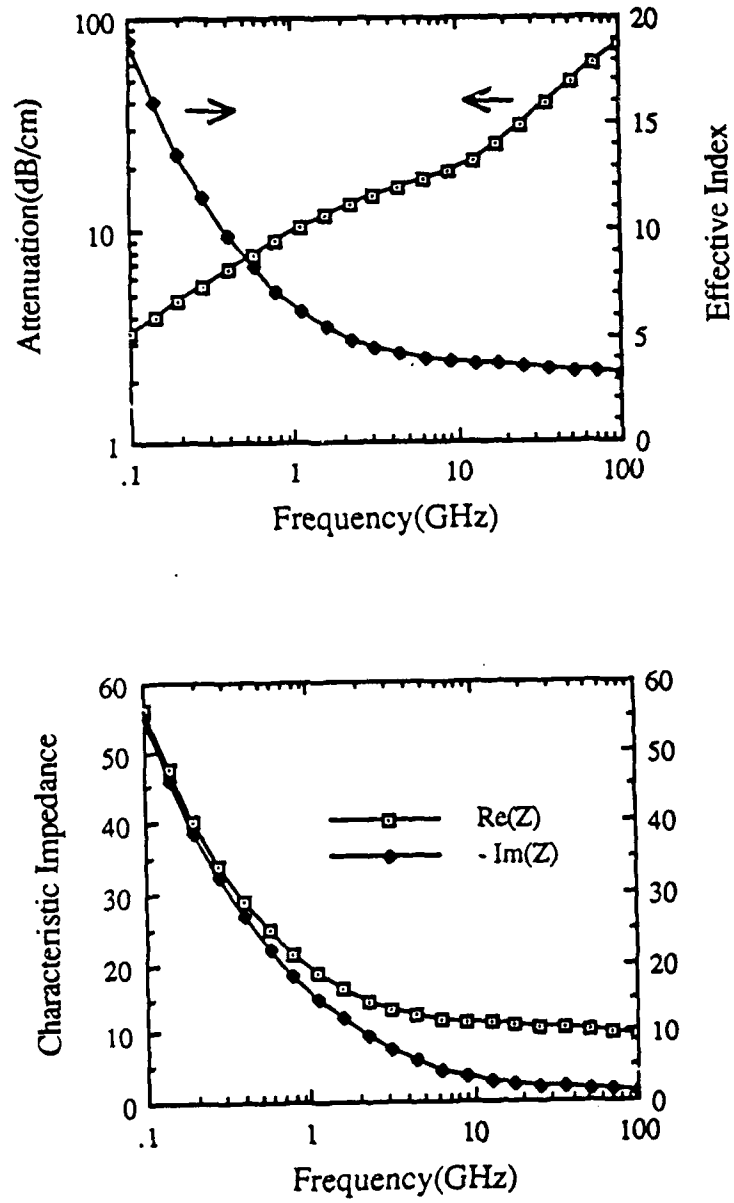
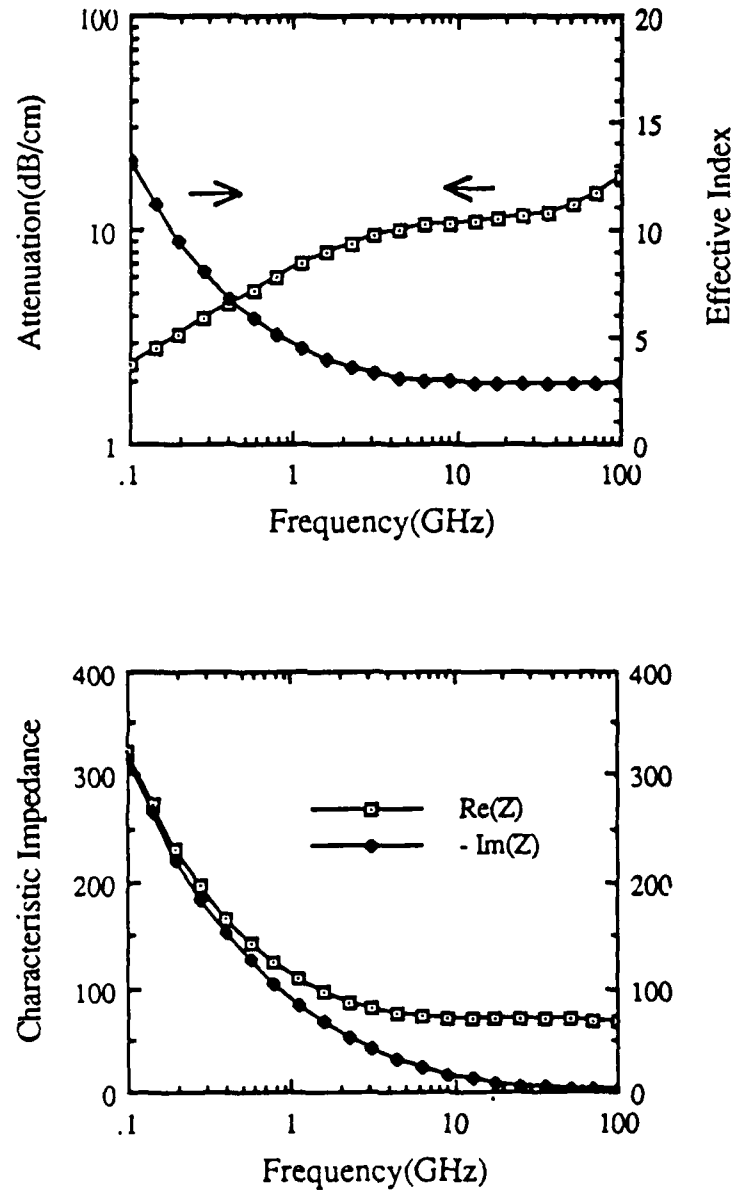Fig. 5. 3. Transmission characteristics of section A

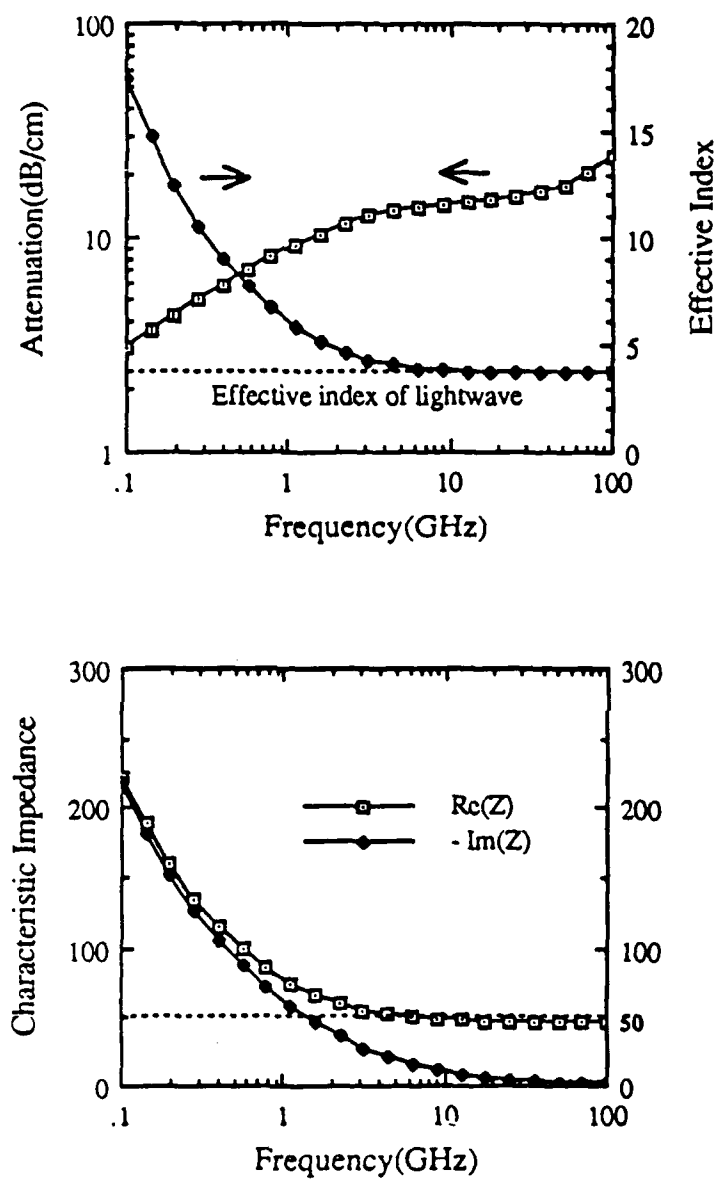Fig. 5. 4. Transmission characteristics of section B

Fig. 5. 5. Transmission characteristics of the slow-wave electrode

In Fig.5.3. and Fig.5.4. are shown the effective indices, the attenuations, and the characteristic impedances of sections A and B, respectively. Section A has much higher conductor loss than that of the coplanar strip structure while section B is designed to have comparable conductor loss using wider electrode gap (8μm). However, since the length of section B (40μm) is much longer than that of section A (5μm), the overall attenuation shown in Fig.5.5. is comparable to that of the coplanar strip structure. The phase velocity of modulation wave and the characteristic impedance are respectively matched to the phase velocity of the optical wave and 50(Ω) in higher frequencies. Fig.5.6. shows the normalized modulation reduction factor defined by the modulation reduction factor divided by that at DC. This coplanar waveguide structurehas the same wide bandwidth (100GHz) as the previous coplanar strip structure, which is much wider than the limit (30GHz) of conventional structures using normal coplanar electrodes as shown in Fig.5.6.
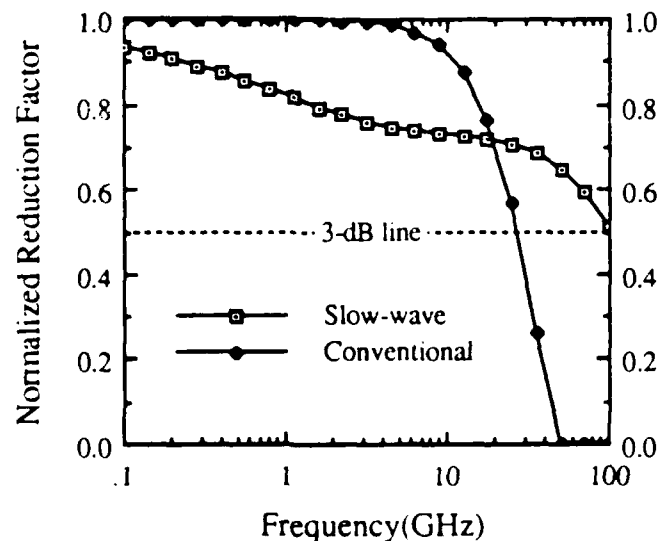
Fig. 5. 6. Normalized modulation reduction factor

The modulation voltage ($V_\pi \approx 38V$) has been calculated approximately from the overlap integral ($\Gamma \approx 0.55$), the electrode gap ($W_B = 8\mu m$), and the ratio of section length ($l_B/l_A = 8$) for the total length ($L = 4mm$). The higher modulation voltage comes from the wider electrode gap which is designed to reduce the high conductor loss in section B. The figure-of-merit is about 2.6 GHz/V which is still higher than those of conventional structures.

5.6. Conclusion

In this chapter, a GaAs traveling-wave optical modulator using a modulated coplanar waveguide electrode with cross-tie overlays has been described. This structure has simultaneous matching of the phase velocity and the impedance and behaves as a uniform transmission line over a wide bandwidth. Also presented is the design method including design considerations for the optimum structure. This coplanar waveguide structure has been analyzed using the spectral domain analysis for each section and by an application of the Floquet's theorem to the periodic array. The dominant conductor loss has been reduced using the modulation of the center strip and calculated by the proposed phenomenological loss equivalence method[44]-[46]. Since this coplanar waveguide structure has higher conductor loss in section B than the coplanar strip structure, it has higher modulation voltage (38 V) for the design of 100 GHz-bandwidth resulting in lower figure-of-merit (2.6 GHz/V). Since this optical modulator has two optical waveguides between the center conductor and two half ground planes, this structure will be suitable for amplitude modulators such as interferometer or coupled-waveguide modulator.

Chapter 6

Conclusion

GaAs traveling-wave optical modulators using coplanar slow-wave electrodes as well as wideband feeding of coplanar strip electrode are described in this technical report. In these structures, the phase velocity matching has been satisfied over a very wide bandwidth by reducing the phase velocity of the modulation wave using the slow-wave electrode. Therefore, the modulation bandwidths are greatly increased while the dominant conductor losses are relatively high and limit the bandwidths. The high conductor losses are reduced by periodically modulating the electrode geometries. The figure-of-merits, the bandwidth divided by the modulation voltage, are much higher than those of conventional structures because of the successful matching of the phase velocity. Therefore, because of the wide bandwidths and high figure-of-merits, these structures have high potential of ultra-high speed light modulation required for next-generation light communication, especially for high-speed heterodyne light communication.

The GaAs traveling-wave optical modulator using the coplanar strip slow-wave electrode has been analyzed using the quasi-static analysis and the proposed phenomenological loss equivalence method in the wide ranges of frequency and field penetration. Optimization of the structure has been carried out by maximizing the figure-of-merit for 4mm-long device at $1.3\mu m$ light wavelength. The maximum 3-dB

85

bandwidth of 100 GHz has been obtained which is much wider than the bandwidth limit (30 GHz) of conventional structures limited by the phase velocity mismatch. Although the calculated modulation voltage of 23 V is a little higher than that (20 V) of a conventional structure due to the slightly lower field overlap in section A, the overall figure-of-merit (4 GHz/V) is much larger than that (1.5GHz/V) of the conventional structure. The slow-wave structure has been build on a semi-insulating GaAs substrate and measured using a microwave network analyzer. The measured effective index (n_{eff}^m=4.61) is much larger than that (n_{eff}^m=2.65) of conventional coplanar electrodes and agrees very well with the calculated one (n_{eff}^m=4.25). The slight deficiency mainly comes from a discontinuity capacitance between the cross-tie section and the normal coplanar strip section which enhances the slow-wave effect.

The coplanar waveguide slow-wave electrode has been analyzed using the spectral domain analysis for each section and by an application of the Floquet's theorem to the periodic array. The dominant conductor loss reduced using the modulation of the center strip and calculated by the phenomenological loss equivalence method. Also presented is the design method including design considerations for the optimum structure. Since this coplanar waveguide structure has higher conductor loss than the coplanar strip structure in section B, it has higher modulation voltage (38 V) for the design of 100 GHz-bandwidth resulting in the lower figure-of-merit (2.6 GHz/V). Since this optical modulator has two optical waveguides between the center conductor and two half ground planes, this structure will be suitable for amplitude modulators such as interferometer or coupled-waveguide modulator.

Wideband feedings of the traveling-wave modulators are required to maintain the modulator bandwidths in practical usage. A new and practical coplanar strip feed of wideband and low return loss has been developed using an intermediate microstrip line between the coplanar strip electrode and a feeding coax which reduces the unbalancing effect and the reflection at the feeding transition. The measured and calculated return losses are in good agreement and below 13 dB up to 18GHz. The extended calculation of the return loss based on the equivalent circuit and the parameters calculated from TDR measurement, shows the return loss below 10dB up to 30GHz. In addition, this structure can be integrated monolithically with the optical devices on a GaAs substrate.

References

[1]   K. Kishino, S. Aoki, and Y. Suematsu, " Wavelength variation of 1.6μm wavelength buried heterostructure GaInAsP/InP lasers due to direct modulation," IEEE J. Quantum Electronics, Vol. QE-18, pp. 343-351, 1982.

[2]   R. A. Linke, " Direct gigabit modulation of injection lasers: Structure dependent speed limitations," J. Lightwave Technology, Vol. LT-2, pp. 40-43, 1984.

[3]   F. S. Chen, " Modulators for optical communications," Proc. IEEE, Vol. 58, No. 10, pp. 1440-1457, October 1970.

[4]   R. C. Alferness, " Waveguide electrooptic modulators," IEEE Trans. Microwave Theory Tech., Vol. MTT-30, pp. 1121-1137, August 1982.

[5]   S. H. Lin, S. Y. Wang, and Y. M. Houng, " GaAs p-i-n electrooptic traveling-wave modulator at 1.3 μm," Electronic Letters, V-20, pp. 934-935, 1986.

[6]   K. Atsuki and E. Yamashita, " Transmission line aspects of the design of broadband electrooptic traveling-wave modulators," J. of Lightwave Tech., Vol. LT-5, pp. 316-319, March 1987.

[7]   M. Nazarathy, D. W. Dolfi, and R. J. Jungerman, " Spread spectrum frequency response of coded phase reversal traveling wave modulators," J. Lightwave Technol., Vol. LT-5, No. 10, pp. 1433-1443, October 1987.

[8] S. Y. Wang, S. H. Lin, and Y. M. Houng, " GaAs traveling-wave polarization electro-optic waveguide modulator with bandwidth in excess of 20 GHz at 1.3 μm," Appl. Phys. Lett., 51(2), 13, pp.83-85, July 1987.

[9] S. Y. Wang and S. H. Lin, " High speed III-V electrooptic waveguide modulators at $\lambda=1.3\mu m$," J. Lightwave Technol., Vol. LT-6, No. 6, pp. 758-771, June 1988.

[10] H. Hasegawa, M. Furukawa, and H. Yanai, " Properties of MIS line on Si-SiO$_2$ system," IEEE Trans. Microwave Theory Tech., Vol. MTT-19, pp. 869-881, 1971.

[11] Y. Fukuoka, Y.-C. Shih, and T. Itoh, " Analysis of slow-wave coplanar waveguide for monolithic integrated circuits," IEEE Trans. Microwave Theory Tech., Vol. MTT-31, pp. 567-573, 1983.

[12] C. M. Krowne and R. E. Neidert, " Slow-wave monolithic variable phase shifter," 10th Int. Conf. Infrared and Millimeterwaves, Lake Buena Vista, FL, pp. 275-276, December 1985.

[13] S. Seki and H. Hasegawa, " Cross-tie coplanar waveguide on semi-insulating GaAs substrate," Electronic Letters, Vol.-17, No. 25, pp. 940-941, December 10, 1981.

[14] T. H. Wang and T. Itoh, " Compact grating structure for application to filters and resonators in monolithic microwave integrated circuits," IEEE Trans. Microwave Theory Tech., Vol. MTT-35, pp. 1176-1182, 1987.

[15] Y.-D. Lin and T. Itoh, " Analysis and improvement of the cross-tie overlay slow-wave structure," submitted to J. Electromagnetic Wave Analysis.

[16] R. E. Collin, Field theory of guided waves, Mcgraw-Hill Book Company, New York (1960).

[17] H.-Y. Lee and T. Itoh, " Wideband GaAs traveling-wave optical modulator using a modulated coplanar strip electrode with cross-tie overlay," 13th Int. Conf. Infrared and Millimeterwaves, Hawaii, pp. 21-22, December 1988.

[18] H.-Y. Lee and T. Itoh, " GaAs traveling-wave optical modulator using a modulated coplanar strip electrode with periodic cross-tie overlays," International J. of Infrared and Millimeterwaves, Vol. 10, No. 3, pp. 321-335, March 1989.

[19] E. Kapan and R. Bhat, " Low-loss single-mode GaAs/AlGaAs optical waveguides grown by organometallic vapor phase epitaxy," Applied Physics Letters, APL-50(23), pp. 1628-1630, June 1987.

[20] K. C. Gupta, R. Garg, and I. J. Bahl, Microstrip lines and slotlines, Artech House, Inc., (1979).

[21] T. Tamir, Integrated optics, Springer-Verlag, NY(1975).

[22] R. C. Jones, " New calculus for the treatment of optical system," J. Optical Society of America, Vol.-31, pp. 488, 1941.

[23] W. R. Cook, Jr. and H. Jaffe, Electro-optic coefficients, Landolt-Bornstein, New Series, K.-H. Hellwege, Ed., Vol.-11, pp.532-651, Springer-Verlag(1979).

[24] C. P. Wen, " Coplanar waveguide : A surface strip transmission line suitable for non-reciprocal gyromagnetic device application," IEEE Trans. Microwave Theory Tech., Vol. MTT-17, pp. 1087-1090, 1969.

[25] M. E. Davis et. al., " Finite-boundary corrections to the coplanar waveguide analysis," IEEE Trans. Microwave Theory Tech., Vol. MTT-21, pp. 594-596, 1973.

[26] A. A. Oliner, S. -T. Peng, T. -I. Hsu, A. Sanchez, " Guidance and leakage properties of a class of open dielectric waveguides: Part II - New Physical Effects," IEEE Trans. Microwave Theory Tech., Vol. MTT-29, pp. 855-869, 1981.

[27] D. Marcuse, Theory of dielectric optical waveguide, Academic Press, NY(1974).

[28] K. Kubota, J. Noda, and O. Mikami, " Traveling-wave optical modulator using a directional coupler LiNbO$_3$ waveguide," J. Quantum Electronics. Vol. QE-16, No.7, pp. 754-760, July 1980.

[29] J. B. Knorr, " Slot-line transitions," IEEE Transactions on Microwave Theory and Techniques, MTT-22 , pp. 548-554, 1974.

[30] H.-Y. Lee and T. Itoh, " Wideband and low return loss coplanar strip feed using intermediate microstrip," Electronics Letters, Vol. 24, No.19, pp. 1207-1208, 15th September 1988.

[31] D. Chambers, S. B. Cohn, E. G. Cristol, and F. Young, " Microwave active network synthesis," Stanford Res. Inst., Menlo Park, Calif., Semiannual Rep., Contract DAAB07-C-0044, SRI Project 8254, 1970.

[32] S. B. Cohn, " Slot line on a dielectric substrate," IEEE Transactions on Microwave Theory and Techniques, MTT-17, pp. 768-778, 1969.

[33] P. Silvester and P. Benedek, " Equivalent capacitances of microstrip open circuits," IEEE Transactions on Microwave Theory and Techniques, MTT-20, pp. 511-516, 1972.

[34] M. L. Majewski, R. W. Rose, and J. R. Scott, " Modeling and characterization of microstrip-to-coaxial transitions," IEEE Transactions on Microwave Theory and Techniques, MTT-29, pp. 799-805, 1981.

[35] H. A. Wheeler, " Formulas for the skin effect," Proceedings of IRE, Vol. 30, pp. 412-424, 1942.

[36] H.-Y. Lee, T.H. Wang, and T. Itoh, " Cross-tie slow-wave structure for broadband traveling-wave type electro-optical modulators," 12th IEEE Int. Conf. Infrared and Millimeterwaves, Orlando, pp. 95-96, December 1987.

[37] H.-Y. Lee, T.H. Wang, and T. Itoh, " Cross-tie slow-wave structure for broadband traveling-wave type electro-optical modulators," Int. Journal of IR and MM Waves, Vol. 9, No.1, pp. 87-99, January 1988.

[38] T. Itoh, " Spectral domain immittance approach for dispersion characteristics of generalized printed transmission lines," IEEE Transactions on Microwave Theory and Techniques, MTT-28, pp. 733-736, 1980.

[39] J. C. Tracy, W. Wiegman, R. A. Logan, and F. K. Reinhart, " Three-dimensional light guides in single-crystal GaAs-$Al_xGa_{1-x}As$," Applied Physics Letters, APL-22, No. 10, pp. 511-512, May 1973.

[40] R. Mittra and S. W. Lee, Analytical techniques in the theory of guided waves, pp. 4-11, New York Macmillan (1971).

[41] R. H. Jansen, " Unified user oriented computation of shielded, covered, and open planar microwave and millimeter-wave transmission line characteristics," Microwaves, Optics, and Acoustics, Vol. MOA-1, pp. 14-22, January 1979.

[42] S. Adachi, " GaAs, AlAs, and $Al_xGa_{1-x}As$: Material parameters for use in research and device applications," J. Applied Physics, Vol.-58(3), pp. R1-R29, August 1985.

[43] E. A. J. Marcatili, " Dielectric rectangular waveguide and directional coupler for integrated optics," Bell System Technical Journal, pp. 2071-2102, September 1969.

[44] H.-Y. Lee and T. Itoh, " Phenomenological loss equivalence method for planar quasi-TEM transmission line with a thin normal conductor or superconductor, " IEEE Trans. Microwave Theory Tech., Vol. MTT-37, Number 12, December 1989.

[45] H.-Y. Lee and T. Itoh, " Wideband conductor loss calculation of planar quasi-TEM transmission lines with thin conductors using a phenomenological loss equivalence method," IEEE International Microwave Symposium, Long Beach, California, pp. 367-370, June 1989.

[46] H.-Y. Lee, K.-S. Kong, T. Itoh, " Conductor loss calculation of superconducting microstrip line using a phenomenological loss equivalence method," 19th European Microwave Conference, London, England, September 1989.

[47] I. J. Bahl and R. Garg, " Simple and accurate formulas for a microstrip with finite strip thickness," Proc. IEEE, Vol. 65, pp. 1611-1612, November 1977.